Capilla Romá, MT.; Talavera Usano, CF.; Ginestar Peiro, D.; Verdú Martín, GJ. (2020). Validation of the SHNC time-dependent transport code based on the spherical harmonics method for complex nuclear fuel assemblies. Journal of Computational and Applied Mathematics. 375:1-21. https://doi.org/10.1016/j.cam.2020.112814

Validation of the SHNC time-dependent transport code based on the spherical harmonics method for complex nuclear fuel assemblies

M. T. Capilla[a,*], C. F. Talavera[a], D. Ginestar[a], G. Verdú[b]

[a]*Departamento de Matemática Aplicada. Universitat Politècnica de València. Camino de Vera 14. E-46022 Valencia, Spain.*
[b]*Instituto de Seguridad Industrial, Radiofísica y Medioambiental. Universitat Politècnica de València. Camino de Vera 14. E-46022 Valencia, Spain.*

Abstract

The diffusion approximation to the time-dependent Boltzmann transport equation gives accurate results for traditional nuclear reactor designs, but new reactor designs and new fuel elements require neutron transport methods. We develop a numerical approximation to the time-dependent transport equation coupled to delayed neutron precursors based on the spherical harmonics P_L equations, for odd L, and on the Backward Euler finite difference discretization of time. The resulting scheme can be written as a stationary form of diffusive second order P_L equations. This allows a reduction by half to the number of unknowns and also to apply a nodal collocation method to the spatial discretization of the problem, using coarse spatial grids to further reduce memory requirements. This scheme is validated with several transient benchmarks, where the convergence properties are established and compared with the simplified P_L approximation. A more realistic transient benchmark, based on the two-group C5 MOX problem, is finally introduced, showing the need of high order P_L approximation for complex fuel geometries.

Keywords: Transient neutron transport equation; Spherical harmonics method; Multi-dimensional P_L equations; Nodal collocation method; Implicit Euler method; C5 MOX transient benchmark.

1. Introduction

The modeling and simulation of transients in a nuclear reactor is mostly based on the time dependent neutron diffusion equation, giving accurate enough results for traditional reactor designs. But now, there is a growing interest in the study of new reactor designs and the use of new fuel elements for which the use of the diffusion approximation may not be accurate enough. This and the advances in computational power, have stimulated the need of using neutron transport methods to analyze reactor kinetics.

*Corresponding author. Tel.: 34-963877630; fax: 34-963877639.
Email addresses: tcapilla@mat.upv.es (M. T. Capilla), talavera@mat.upv.es (C. F. Talavera), dginesta@mat.upv.es (D. Ginestar), gverdu@iqn.upv.es (G. Verdú)

Except for very simple problems, the direct solution of the Boltzmann neutron transport equation [1] is not feasible because it is an integro-differential equation involving fields defined in seven dimensions: three for space, two describing a direction in the unit sphere of the incident neutrons, one for the energy and one for the time. Hence, the development of numerical methods that give accurate solutions to the time dependent neutron transport equation in 3D geometry is still a very challenging problem [2].

The energy dependence is usually modeled with the multigroup approximation, where the energy-line is divided into discrete energy groups; this approximation reduces the continuous problem to g monoenergetic problems that are coupled through the source term, where the fission, down-scattering and up-scattering processes are taken into account.

There are several techniques to deal with the angular dependence of the Boltzmann transport equation. One possibility is the use of the spherical harmonics method, where the angular dependence of the angular neutronic flux and the nuclear cross-sections are expanded as a finite series in terms of the spherical harmonics functions, leading to the P_L approximations of the neutron transport equation (see [3, 4, 5, 6]). The resulting equations preserve the rotational symmetry of the transport equation, and the incorporation of anisotropic scattering and sources (internal and external) can be done in a natural way.

The classical diffusion equation was developed assuming isotropy for the neutronic flux and the nuclear cross-sections, but this approximation only works well when some simplifying assumptions are satisfied [7]. Also, the parabolic nature of the diffusion equation predicts that particles have an infinite velocity and so fails near strong absorbers like fuel bundles and control rods. The classical P_1 approximation (the "telegrapher equation") has a finite particle velocity but with the wrong value. To correct this drawback it is necessary to formulate an asymptotic new approximation, which includes the correct time behaviour for a general medium [8].

The simplified P_L (SP_L) approximation was initially developed in 1960 to reduce the number of unknowns that appear in the P_L spherical harmonics equations [9, 10], thus reducing the complexity, the storage and the computational time of the full P_L approximation. The SP_L equations where originally based on the P_L 1D equations and developed for steady-state problems. Later, it was showed [11] that the SP_L equations can be understood as an asymptotic approximation of the P_L equations. These equations have been successfully applied to other fields [12] and extended to time-dependent problems [13].

The discrete ordinates S_N method [14, 15], that consists on evaluating the angular flux and the nuclear cross-sections at discrete angular directions, is characterized by a set of quadrature points. Some numerical codes based on this methodology are DANTSYS [16] and PARTISN [17].

The method of characteristics (MOC) [18, 19] is based on the construction of a large enough number of characteristic lines or rays, along which the transport equation is solved. This method was traditionally used to solve static problems, but it has been extended to perform transient calculations [20, 21].

The Monte Carlo approximation has been recently proposed to solve the time-dependent neutron transport equation [22, 23, 24, 25], handling the time variation of the neutron flux updating event times during the Monte Carlo neutron tracking.

Other important aspect to consider in reactor kinetics methods for neutron transport is the time dependence approximation. Usually, a backward finite difference scheme is used for the time derivative leading to an unconditionally stable implicit method. Although this is the most common technique, a high-order approximation has been used [26] for the angular flux time derivative, and a similar method was used in [27] for the neutron diffusion approximation. Also,

high order discretization using Runge-Kutta methods are presented in [28]. Other possibilities are a quasi-static method [29] or schemes based on modal approximations [30, 31].

We can see that during the last years considerable efforts have been made in the development of numerical methods applied to space-time nuclear reactor transient modeling, using higher order approximations to the neutron transport equation. In this line, we have extended our developments based on the P_L equations [5, 6] to the time domain. For the time discretization of the equations we have used the backward Euler finite difference approximation. The main advantage of our approach is the reduction by half of the size of the system of equations that has to be solved at each time step of the implicit method. This is achieved by including the odd field equations and the neutron precursor equations into the even field equations, resulting into a vector-valued stationary diffusive equation for the even fields with source and diffusion terms that incorporates the odd fields and the neutron precursors. An additional advantage results from the diffusive nature of the equations, where the spatial discretization is performed with a nodal collocation method, based on a finite expansion in terms of orthonormal Legendre polynomials. This method, initially developed in [32] and generalized in [5, 6] to arbitrary odd order L, efficiently achieves accurate results using a coarse spatial mesh, thus reducing memory requirements. Finally, an approximation based on the SP_L approximation is also evaluated, consisting in removing cross-derivative terms from the general P_L formulation. Its results are compatible with the standard SP_L implementations as given for example in [33], showing that for diffusive-like problems improves P_1 calculations but, on the other hand, for high spatial gradients differences become larger and the approximation is inaccurate.

The remainder of the paper is organized as follows. In Section 2 we describe the discretization method that is applied to the time dependent Boltzmann transport equation and the delayed neutron precursor equations. The spherical harmonics method is reviewed, and its application gives the P_L equations; the method is also applied to boundary conditions: Marshak's vacuum and external source, reflective and zero-flux. The time discretization is then performed with a backward Euler method, and it is shown that the resulting problem can be reduced to an implicit problem for a second order diffusive P_L equation for the even fields and two explicit equations for the odd fields and the neutron precursor families. The nodal collocation method is then used for these equations. In Section 3, this numerical scheme is validated in some test cases. The convergence of the method is first studied in a simple 1D homogeneous slab problem with analytical solution, with physical parameters chosen to show significant differences between the diffusive approximation and the transport theory. The next two problems are well described by the diffusion approximation: a 1D subcritical transient benchmark with three different materials, two energy groups and six delayed neutron families, and two 2D TWIGL transient reactor problems based on a linear ramp and on a step reactivity perturbation. The last case is based on a C5 MOX benchmark transient that shows strong spatial gradients thus requiring high order P_L methods to accurately track the neutron flux distribution at the pin level. In Section 4, we establish our Conclusions.

2. The transport equation and the P_L equations

2.1. The Boltzmann transport equation

The neutron interactions in the interior of a general reactor core can be modeled by the Boltzmann transport equation [7] and by a set of neutron precursor equations. The time-dependent

transport equation, in terms of the independent variables position $\vec{r}$, direction $\vec{\Omega}$, energy E and time t is given by:

$$\frac{1}{v(E)}\frac{\partial\Phi}{\partial t}(\vec{r},\vec{\Omega},E,t) + \vec{\Omega}\,\vec{\nabla}\Phi(\vec{r},\vec{\Omega},E,t) + \Sigma_t(\vec{r},E,t)\,\Phi(\vec{r},\vec{\Omega},E,t)$$
$$= S_s(\vec{r},\vec{\Omega},E,t) + S_f(\vec{r},\vec{\Omega},E,t) + S_d(\vec{r},t) + S(\vec{r},\vec{\Omega},E,t)\,, \quad \vec{r}\in V\,, \quad (1)$$

where $\Phi(\vec{r},\vec{\Omega},E,t)$ is the neutron angular flux; V is the core volume; $\vec{v}(E)$ is the neutron velocity, $v(E) = |\vec{v}(E)|$, and $E = mv^2/2$ is the kinetic energy for a neutron of mass m; $\vec{\Omega} = \vec{v}/|\vec{v}| = (\cos\varphi\,\sin\theta\,,\,\sin\varphi\,\sin\theta\,,\,\cos\theta)$, $0<\varphi<2\pi$, $0<\theta<\pi$, is the neutron direction unit vector and Σ_t is the total macroscopic cross-section. The right hand side of (1) describes the neutron sources that include the scattering source term S_s, the source of neutrons by fission term S_f, the delayed neutron source S_d and the fixed source term S, given by

$$S_s(\vec{r},\vec{\Omega},E,t) = \int dE' \int d\vec{\Omega}'\,\Sigma_s(\vec{r};\vec{\Omega}',E'\to\vec{\Omega},E)\,\Phi(\vec{r},\vec{\Omega}',E',t)\,,$$
$$S_f(\vec{r},\vec{\Omega},E,t) = \frac{1}{4\pi}(1-\beta)\chi_p(\vec{r},E)\int dE'\,\nu\Sigma_f(\vec{r},E',t)\int d\vec{\Omega}'\,\Phi(\vec{r},\vec{\Omega}',E',t)\,,$$
$$S_d(\vec{r},t) = \frac{1}{4\pi}\sum_{j=1}^{N_d}\chi_{d,j}(\vec{r},E)\lambda_j C_j(\vec{r},t)\,.$$

Here $d\vec{\Omega} = \sin\theta\,d\varphi d\theta$, Σ_s is the scattering cross-section from $(\vec{\Omega}',E')$ to $(\vec{\Omega},E)$, Σ_f is the fission cross-section, ν is the average number of neutrons per fission, χ_p is the prompt neutron fission spectrum, $\beta = \sum_{j=1}^{N_d}\beta_j$ is the total delayed neutron fraction, and the delayed magnitudes for precursor group j are: the neutron spectrum $\chi_{d,j}$, the decay constant λ_j, and the neutron fraction β_j (the last two are energy independent). Finally, C_j is the delayed neutron precursor concentration for precursor group $j = 1,\ldots,N_d$, that satisfies the differential equation

$$\frac{\partial C_j}{\partial t}(\vec{r},t) = -\lambda_j C_j(\vec{r},t) + \beta_j\int dE'\int d\vec{\Omega}'\,\nu\Sigma_f(\vec{r},E',t)\,\Phi(\vec{r},\vec{\Omega}',E',t)\,. \quad (2)$$

For steady state problems $\frac{\partial\Phi}{\partial t} = \frac{\partial C_j}{\partial t} = 0$, and the stationary delayed neutron precursor concentration can be obtained from Eq. (2),

$$\lambda_j C_j^{\text{stat}}(\vec{r}) = \beta_j\int dE'\int d\vec{\Omega}'\,\nu\Sigma_f(\vec{r},E')\,\Phi^{\text{stat}}(\vec{r},\vec{\Omega}',E')\,, \quad (3)$$

that, inserted into Eq. (1), gives the equation that must satisfy the stationary neutron flux Φ^{stat}:

$$\vec{\Omega}\,\vec{\nabla}\Phi(\vec{r},\vec{\Omega},E) + \Sigma_t(\vec{r},E)\,\Phi(\vec{r},\vec{\Omega},E)$$
$$= S_s(\vec{r},\vec{\Omega},E) + S_f^{\text{stat}}(\vec{r},\vec{\Omega},E) + S(\vec{r},\vec{\Omega},E)\,, \quad \vec{r}\in V\,, \quad (4)$$

where

$$S_f^{\text{stat}}(\vec{r},\vec{\Omega},E,t) = \frac{1}{4\pi}\chi_p^{\text{stat}}(\vec{r},E)\int dE'\,\nu\Sigma_f(\vec{r},E')\int d\vec{\Omega}'\,\Phi(\vec{r},\vec{\Omega}',E')\,,$$

with $\chi_p^{\text{stat}}(\vec{r},E) = (1-\beta)\chi_p(\vec{r},E) + \sum_{j=1}^{N_d}\chi_{d,j}(\vec{r},E)\beta_j$.

Any of these equations must be supplemented with appropriate boundary conditions. Among others, we will consider the following:

1. If an *external source* $T(\vec{r},\vec{\Omega},E,t)$ is located at the boundary surface ∂V of the reactor, then the angular neutronic flux satisfies

$$\Phi(\vec{r},\vec{\Omega},E,t) = T(\vec{r},\vec{\Omega},E,t)\,, \quad \text{for all } \vec{\Omega}\,\vec{n} \le 0\,,\ \vec{r}\in\partial V\,,\ t\ge 0\,, \tag{5}$$

   for every incoming direction ($\vec{n}$ is the normal vector pointing outward to the external surface). As a particular case, when the incoming flux is zero, $T = 0$, we obtain vacuum boundary conditions.
2. *Reflective boundary conditions* appear when the same physical conditions occur at both sides of a symmetry plane, and then the neutronic flux verifies

$$\Phi(\vec{r},\vec{\Omega},E,t) = \Phi(\vec{r},\vec{\vec{\Omega}},E,t)\,, \tag{6}$$

   where $\vec{\vec{\Omega}}$ is the angular direction of the reflected neutron with respect to the symmetry plane.
3. *Zero flux boundary conditions* are set when the boundary is far away from fission sources and the angular neutronic flux is (almost) null $\Phi \simeq 0$.

2.2. Angular discretization. The spherical harmonics method

The first approximation to numerically solve Eq. (4) is to replace the continuous variable E by a discretization into a finite number of energy groups $g \in G$, where group g spans the range of energies from E_g to E_{g+1}. This is known as the energy multi-group approximation. For simplicity of the notation we will assume that there is one energy group in the developments that follow. It is easy to extend the results to an arbitrary number G of energy groups, where now $\Phi(\vec{r},\vec{\Omega},E,t)$ is a vector of G components, and Σ_t, Σ_s, $\nu\Sigma_f$ are matrices with respect to the energy group indices.

The angular dependence of the neutronic flux $\Phi(\vec{r},\vec{\Omega},t)$ and the source term $S(\vec{r},\vec{\Omega},t)$ is developed in terms of spherical harmonics

$$\begin{aligned}
\Phi(\vec{r},\vec{\Omega},t) &= \sum_{l=0}^{\infty}\sum_{m=-l}^{+l} \phi_{lm}(\vec{r},t)\, Y_l^m(\vec{\Omega})\,,\\
S(\vec{r},\vec{\Omega},t) &= \sum_{l=0}^{\infty}\sum_{m=-l}^{+l} s_{lm}(\vec{r},t)\, Y_l^m(\vec{\Omega})\,,
\end{aligned} \tag{7}$$

where $Y_l^m(\vec{\Omega}) = H_l^m\, P_l^m(\cos\theta) e^{im\varphi}$ are the (complex) spherical harmonics [34] ($P_l^m(\cos\theta)$ are the associated Legendre polynomials and the coefficients $H_l^m = \sqrt{(2l+1)/(4\pi)}\cdot\sqrt{(l-m)!/(l+m)!}$, that form a complete set of orthonormal functions satisfying the orthonormality property $\int d\vec{\Omega}\, {Y_m^l}^* Y_{m'}^{l'} = \delta_{ll'}\delta_{mm'}$, where δ_{ij} is the Kronecker delta.

Thus, the unknowns of Eq. (1) are the (spherical harmonics) moments $\phi_{lm}(\vec{r},t)$ and, given that we are interested in real solutions of the (real) transport equation (1), then $\Phi = \Phi^*$, that is, ${\phi_{lm}}^* = (-1)^m \phi_{l,-m}$ and not all complex coefficients are independent, then there are only $2l+1$ real independent moments for each $l > 0$, that is, $\{\phi_{l0}, \mathrm{Re}\,\phi_{lm}, \mathrm{Im}\,\phi_{lm}, m = 1,\ldots,l\}$.

Based on physical grounds, the scattering is supposed to depend on the relative angle $\vec{\Omega}\,\vec{\Omega}'$ between the incident and the scattered particles, and then the scattering cross-section may be modelled by the Legendre polynomials series

$$\Sigma_s(\vec{r},\vec{\Omega}\,\vec{\Omega}') = \sum_{l=0}^{\infty} \frac{2l+1}{4\pi}\Sigma_{s,l}(\vec{r})\, P_l(\vec{\Omega}\,\vec{\Omega}')\,. \tag{8}$$

Expansions (7) and (8) and the orthogonality properties of Y_l^m are then used into Eq. (1). To achieve a finite approximation, the expansions given by series (7) and (8) are truncated at some finite order $l = L$, i.e., $\phi_{lm} = s_{lm} = 0$, for $l > L$ (the so-called P_L closure condition [35]) and the resulting equations are the P_L equations, see for example [36, 6, 37] for a full development. In the following, we will only consider L to be an odd integer because, as a consequence of the interface conditions given by Eqs. (13), the even order moments are continuous functions and, in particular, the neutronic scalar flux $\int \Phi \, d\vec{\Omega} = \sqrt{4\pi}\,\phi_{00}$ is continuous along the reactor volume.

Defining the real moments

$$\begin{aligned} \xi_{lm} &= \mathrm{Re}\,\phi_{lm} = \frac{1}{2}(\phi_{lm} + (-1)^m \phi_{l,-m}), \quad l = 0, 1, \ldots, L, \\ \eta_{lm} &= \mathrm{Im}\,\phi_{lm} = \frac{1}{2i}(\phi_{lm} - (-1)^m \phi_{l,-m}), \quad l = 1, \ldots, L, \end{aligned} \tag{9}$$

and gathering even l moments into vectors $X = (\xi_{l,m\geq 0}, \eta_{l,m>0})_{l=\mathrm{even}}$ and $\mathcal{S} = (\mathrm{Re}\, s_{l,m\geq 0}, \mathrm{Im}\, s_{l,m>0})_{l=\mathrm{even}}$, with $n_e = L(L+1)/2$ components when L is odd, and odd l moments into vectors $\bar{X} = (\xi_{l,m\geq 0}, \eta_{l,m>0})_{l=\mathrm{odd}}$ and $\bar{\mathcal{S}} = (\mathrm{Re}\, s_{l,m\geq 0}, \mathrm{Im}\, s_{l,m>0})_{l=\mathrm{odd}}$, with $n_o = (L+1)(L+2)/2 = n_e + L + 1$ components (for example, if $L = 1$ then $X = (\xi_{00})$ and $\bar{X} = (\xi_{10}, \xi_{11}, \eta_{11})^T$), then the P_L equations can be expressed as a set of real vector-valued first order differential equations

$$\begin{aligned} &\frac{1}{v}\frac{\partial X}{\partial t} + \sum_{j=1}^{3} M_j \frac{\partial \bar{X}}{\partial x_j} + \Sigma_a X \\ &\quad = (1-\beta)\chi_p \,\mathrm{diag}(\nu\Sigma_f\, \delta_{l0}\delta_{m0})\, X + \frac{1}{\sqrt{4\pi}} \sum_{j=1}^{N_d} \chi_{d,j}\lambda_j C_j\, \delta_{l0}\delta_{m0} + \mathcal{S}, \end{aligned} \tag{10}$$

$$\frac{1}{v}\frac{\partial \bar{X}}{\partial t} + \sum_{j=1}^{3} \bar{M}_j \frac{\partial X}{\partial x_j} + \bar{\Sigma}_a \bar{X} = \bar{\mathcal{S}}, \tag{11}$$

$$\frac{\partial C_j}{\partial t} = -\lambda_j C_j + \sqrt{4\pi}\beta_j \nu\Sigma_f\, \phi_{00}, \quad j = 1, \ldots, N_d, \tag{12}$$

where (x_1, x_2, x_3) are Cartesian coordinates, $\Sigma_a = \mathrm{diag}(\Sigma_t - \Sigma_{sl})_{l=\mathrm{even}}$, $\bar{\Sigma}_a = \mathrm{diag}(\Sigma_t - \Sigma_{sl})_{l=\mathrm{odd}}$ are square diagonal matrices, and M_j and $\bar{M}_j$ are rectangular matrices (of dimension $n_e \times n_o$ and $n_o \times n_e$, respectively) that are described in previous works [36, 6, 37]. It is worth noting that, due to the definite parity of the spherical harmonics, the even l and odd l moments are the coefficients of the even-parity and odd-parity neutronic flux $\Phi^{\pm} = \frac{1}{2}[\Phi(\vec{\Omega}) \pm \Phi(-\vec{\Omega})] = \sum_{l=\substack{even\\odd}} \sum_{m=-l}^{l} \phi_{lm} Y_l^m$ that appear in the derivation of the even-parity transport equation [38]. See also [39] for a relationship between the even-parity transport equation and the SP_L approximation.

We notice that lower dimensional geometries can be obtained from symmetry constraints to the angular neutronic flux. The XY (2D) geometry describes a medium with cross-sections and source independent of Z direction and equations can be obtained by imposing that the angular neutronic flux does not depend on the third coordinate, $\Phi = \Phi(x_1, x_2, \vec{\Omega}, t)$, so $\frac{\partial \Phi}{\partial x_3} = 0$, and also must satisfy the symmetry relation $\Phi(\theta) = \Phi(\pi - \theta)$, so the moments $\phi_{lm} = 0$ for odd $l + m$ (see later the reflective boundary conditions). The planar (1D) geometry describes a medium that is transversely infinite (in the XY plane) with cross-section and source variation only in the Z direction; this case is obtained by requiring that the neutronic flux $\Phi = \Phi(x_3, \theta, t)$ so the only nonzero moments are $\phi_{l,m=0} = \xi_{l0}$, that are real moments.

At points where the internal source or any cross-section is discontinuous, Eqs. (10) and (11) are undefined, and it is required some sort of *interface conditions* for these regions. We will replace the interface with a very thin transition region, where the physical properties of the medium change rapidly, but continuously [40]. If, for example, the discontinuity occurs along the X axis with coordinate $x_1 = x_{1,0}$, the transition region extends from $x_{1,0} - \Delta$ to $x_{1,0} + \Delta$. On integrating the P_L equations (10) and (11) over the transition region, and taking $\Delta \to 0+$, all integrands remain continuous at the transition region, and the following *interface conditions* are obtained:

$$\begin{aligned} \lim_{\Delta\to 0+} M_1\, \bar{X}(x_{1,0}+\Delta) &= \lim_{\Delta\to 0+} M_1\, \bar{X}(x_{1,0}-\Delta)\,, \\ \lim_{\Delta\to 0+} \bar{M}_1\, X(x_{1,0}+\Delta) &= \lim_{\Delta\to 0+} \bar{M}_1\, X(x_{1,0}-\Delta)\,. \end{aligned} \tag{13}$$

But matrix $\bar{M}_1$, of dimension $n_o \times n_e$ (with $n_o > n_e$ for odd L approximation) has maximum rank, and then second equation in (13) implies continuity of even order moments X at the interface,

$$\lim_{\Delta\to 0+} X(x_{1,0}+\Delta) = \lim_{\Delta\to 0+} X(x_{1,0}-\Delta)\,. \tag{14}$$

On the other hand, as $\dim(M_1) = n_e \times n_o$, the first equation gives n_e linear relations between the n_o ($> n_e$) odd moments $\bar{X}$, so it is not possible to guarantee continuity of *all* the moments.

Boundary conditions are then approximated using the spherical harmonics method as follows:

1. An external source located at the surface boundary (5) requires an approximate treatment. Marshak's approach [7] is based on the conditions

$$\int_{\vec{\Omega}\,\vec{n}\le 0} d\vec{\Omega}\; Y_l^{m*}(\vec{\Omega})\,(\Phi(\vec{r},\vec{\Omega},t) - T(\vec{r},\vec{\Omega},t)) = 0\,, \tag{15}$$

   for $l = 1, 3, 5, \ldots, L$ (odd) and $m = 0, 1, \ldots, l$ (no negative m index is considered because the imposition that the neutronic flux Φ must be real gives redundant conditions). This gives $2l + 1$ real conditions for each odd index l. We will only consider regions with prismatic geometry. If we replace the spherical harmonics expansion (7) for Φ and also for the external source,

$$T(\vec{r},\vec{\Omega},t) = \sum_{l=0}^{\infty} \sum_{m=-l}^{+l} T_{lm}(\vec{r},t) Y_l^m(\vec{\Omega})\,,$$

   truncated up to a finite odd order L, into Marshak's conditions (15), we arrive at the homogeneous system of equations

$$\frac{1}{2}(\phi_{lm} - T_{lm}) + \sum_{\substack{l' \text{ even} \\ -l'\le m'\le l'}}^{L-1} \Big(\int_{\vec{\Omega}\,\vec{n}\le 0} d\vec{\Omega}\; Y_l^{m*}(\vec{\Omega})\, Y_{l'}^{m'}(\vec{\Omega}) \Big) (\phi_{l'm'} - T_{l'm'}) = 0\,, \tag{16}$$

   for $l = 1, 3, 5, \ldots, L$ and $m = 0, 1, \ldots, l$. The real form of (16) allows us to rewrite Marshak's conditions in matrix form

$$\bar{X} + N\,X = \bar{T} + N\,T\,, \tag{17}$$

   where real vectors X and $\bar{X}$ were defined in previous paragraphs, similarly vectors $T = (\mathrm{Re}\, T_{l,m\ge 0}, \mathrm{Im}\, T_{l,m>0})_{l=\text{even}}$, $\bar{T} = (\mathrm{Re}\, T_{l,m\ge 0}, \mathrm{Im}\, T_{l,m>0})_{l=\text{odd}}$, and N is a real rectangular matrix (of dimensions $n_o \times n_e$) with matrix elements

$$N_{(lm),(l'm')} = 2 \int_{\vec{\Omega}\,\vec{n}\le 0} d\vec{\Omega}\; Y_l^{m*}(\vec{\Omega})\, Y_{l'}^{m'}(\vec{\Omega})$$

((lm), l odd, are row indices; ($l'm'$), l' even, are column indices, with appropriate ordering). We treat the discontinuity between the external surface and the interior region by inserting a very thin transition region, as before. If, for example, the boundary surface is located at $x_3 = x_{3,0}$ with normal vector parallel to Z axis, the transition region corresponds to the interval $[x_{3,0}, x_{3,0} + \Delta]$. We obtain the following interface conditions:

$$\begin{aligned} &\lim_{\Delta\to 0+} M_3\,\bar{X}(x_{3,0}+\Delta) = M_3\,\bar{X}(x_{3,0})\,, \\ &\lim_{\Delta\to 0+} X(x_{3,0}+\Delta) = X(x_{3,0})\,, \end{aligned} \tag{18}$$

so X is continuous at the interface but, using Eq. (17), $\bar{X}$ satisfies the interface condition

$$\lim_{\Delta\to 0+} M_3\,\bar{X}(x_{3,0}+\Delta) = M_3\left(-N_3^-\,X(x_{3,0}) + \bar{T}(x_{3,0}) + N_3^-\,T(x_{3,0})\right), \tag{19}$$

that is, a system of n_e linear conditions.

2. Reflective boundary conditions are imposed in an exact way for every finite order L. If, for example, the symmetry plane has normal vector $\vec{n}$ pointing to the negative Z axis, the condition is

$$\Phi(\vec{r},\varphi,\theta,t) = \Phi(\vec{r},\varphi,\pi-\theta,t)\,, \quad \text{for } 0<\varphi<2\pi\,,\ 0<\theta<\pi/2\,. \tag{20}$$

Inserting expansion (7), this equation is equivalent to the following

$$\sum_{l=0}^{\infty}\sum_{m=-l}^{+l}(1-(-1)^{l+m})\,\phi_{lm}(\vec{r})\,Y_l^m(\vec{\Omega}) = 0\,,$$

that is,

$$\phi_{lm} = 0\,, \qquad \text{for } l+m \text{ odd}, \tag{21}$$

for $l = 0, 1, \ldots$ and $m = 0, 1, \ldots, l$. The same conclusion is obtained if the normal vector $\vec{n}$ points to the positive Z axis, and also when we consider a 2D geometry that incorporates the XY symmetry. Finally, for 1D geometry, where the coefficients with index $m \neq 0$ are zero, the symmetry gives the restriction $\phi_{l0} = 0$ for odd l. For a finite L expansion in spherical harmonics, these equations (21) give $L(L+1)/2 = n_e$ conditions. Reflective boundary conditions can also be computed for the other symmetry surfaces, and give the restrictions:

$$\begin{aligned} &\phi_{lm} - (-1)^m\phi^*_{lm} = \phi_{lm} - \phi_{l,-m} = 0\,, && \text{for YZ symmetry surface,} \\ &\phi_{lm} - \phi^*_{lm} = \phi_{lm} - (-1)^m\phi_{l,-m} = 0\,, && \text{for XZ symmetry surface.} \end{aligned}$$

3. Zero flux approximation corresponds to the setting $X \simeq 0$ and $M_1\,\bar{X} \simeq 0$ at external surfaces.

2.3. Time discretization. The Euler implicit method

The large magnitude of the neutron velocities suggests that an unconditionally stable, fully implicit time discretization method can be more favorable, allowing relatively large time steps. Therefore, we will employ a first order backward Euler method, with constant time step Δt, to

discretize the time derivatives in Eqs. (10), (11) and (12). Given the discrete times $t_k = k\Delta t$, $k = 0, 1, \ldots$, then at the interval $[t_{k-1}, t_k]$

$$\frac{1}{v\Delta t}(X^k - X^{k-1}) + \sum_{j=1}^{3} M_j \frac{\partial \bar{X}^k}{\partial x_j} + \Sigma_a^k X^k \tag{22}$$

$$= (1-\beta)\chi_p \,\mathrm{diag}(\nu\Sigma_f^k \delta_{l0}\delta_{m0})\, X^k + \frac{1}{\sqrt{4\pi}} \sum_{j=1}^{N_d} \chi_{d,j}\lambda_j C_j^k \,\delta_{l0}\delta_{m0} + \mathcal{S}^k\,,$$

$$\frac{1}{v\Delta t}(\bar{X}^k - \bar{X}^{k-1}) + \sum_{j=1}^{3} \bar{M}_j \frac{\partial X^k}{\partial x_j} + \bar{\Sigma}_a^k \bar{X}^k = \bar{\mathcal{S}}^k\,, \tag{23}$$

$$\frac{1}{\Delta t}(C_j^k - C_j^{k-1}) = -\lambda_j C_j^k + \sqrt{4\pi}\beta_j \nu\Sigma_f^k \phi_{00}^k\,, \quad j = 1, \ldots, N_d\,, \tag{24}$$

where X^k, $\bar{X}^k$ and C_j^k are the unknowns at time $t_k = k\Delta t$. We also take into account that cross-sections and neutron source can change with time. To achieve an efficient implementation of the above implicit problem, if we define $\tilde{C}_j^k = \lambda_j C_j^k$, the k-th iteration of each precursor concentration in Eq. (24) is

$$\tilde{C}_j^k = (1 + \lambda_j\Delta t)^{-1}(\tilde{C}_j^{k-1} + \lambda_j\Delta t\,\sqrt{4\pi}\beta_j\,\nu\Sigma_f^k\,\phi_{00}^k)\,, \quad j = 1, \ldots, N_d\,, \tag{25}$$

and in the equation for odd order fields (23)

$$\bar{X}^k = D_{\mathrm{eff}}^k\Big(-\sum_{j=1}^{3} \bar{M}_j \frac{\partial X^k}{\partial x_j} + \bar{S}_{\mathrm{eff}}^k\Big), \tag{26}$$

where $D_{\mathrm{eff}}^k = [\bar{\Sigma}_a^k + (v\Delta t)^{-1}]^{-1}$ and $\bar{S}_{\mathrm{eff}}^k = (v\Delta t)^{-1}\bar{X}^{k-1} + \bar{S}^k$, are inserted into Eq. (22) to obtain

$$-\sum_{i,j=1}^{3} \frac{\partial}{\partial x_i}\Big[M_i D_{\mathrm{eff}}^k \bar{M}_j \frac{\partial X^k}{\partial x_j}\Big] + (\Sigma_a^k + (v\Delta t)^{-1})\, X^k - \chi_{\mathrm{eff}}\,\nu\Sigma_f^k\phi_{00}^k\,\delta_{l0}\delta_{m0} = S_{\mathrm{eff}}^k\,, \tag{27}$$

where we have defined the effective magnitudes

$$\chi_{\mathrm{eff}} = \chi_p(1-\beta) + \sum_{j=1}^{N_d} \chi_{d,j}(1 + \lambda_j\Delta t)^{-1}\,\lambda_j\Delta t\beta_j\,,$$

$$S_{\mathrm{eff}}^k = (v\Delta t)^{-1}X^{k-1} + S^k - \sum_{j=1}^{3} M_j \frac{\partial}{\partial x_j}[D_{\mathrm{eff}}^k\,\bar{S}_{\mathrm{eff}}^k] + \frac{1}{\sqrt{4\pi}} \sum_{j=1}^{N_d} \chi_{d,j}(1 + \lambda_j\Delta t)^{-1}\tilde{C}_j^{k-1}\,.$$

We observe the following facts about the numerical method described by these equations:

1. The k-th iteration computes first, using the implicit formula (27) the even order fields X^k from previous iteration data X^{k-1}, $\bar{X}^{k-1}$ and $\tilde{C}_j^{k-1}$. This reduces the dimension of the initial implicit problem (22), (23), (24) by half. Once the updated value of X^k is obtained, the explicit formulas (26) and (25) allow a quick computation of $\bar{X}^k$ and $\tilde{C}_j^k$, $j = 1, \ldots, N_d$.
2. Eq. (27) corresponds to a vector-valued second order stationary form of P_L equation as described in [5, 36, 6] with a modified total cross-section $\Sigma_t + (v\Delta t)^{-1}$ [41], an effective diffusion matrix D_{eff}^k and an effective source term S_{eff}^k that are time-dependent.

3. Eq. (26) relates even order and odd order fields and corresponds to a modified *Fick's law* with an effective diffusion matrix D^k_{eff} and an additional odd order source term $\bar{S}^k_{\text{eff}}$ that are time-dependent.
4. Eqs. (27) and (26) for odd and even order fields are the analogous of the backward-Euler discretized even-parity transport equations (13) and (17) for odd parity and even parity fields described in [38].
5. When the spatial dimension is greater than 1 and we remove cross-derivative terms from Eq. (27), we obtain an approximation similar to the *simplified spherical harmonics* SP_L equations. From now on, we will denote this approximation as the *extended simplified spherical harmonics* equations, ESP_L, and we will show computed results for the problems presented in Sections 3.3 and 3.4.

The time iteration requires an initial state. When the initial state is the *stationary state*, then the even order field X^{stat} is solution of the second order diffusive P_L equation

$$-\sum_{i,j=1}^{3} \frac{\partial}{\partial x_i}\Big[M_i D \bar{M}_j \frac{\partial X}{\partial x_j}\Big] + \Sigma_a X - \chi_p^{\text{stat}} \nu\Sigma_f \phi_{00}\, \delta_{l0}\delta_{m0} = \mathcal{S}^{\text{stat}}, \tag{28}$$

where $D = [\bar{\Sigma}_a]^{-1}$, $\mathcal{S}^{\text{stat}} = \mathcal{S} - \sum_{j=1}^{3} \frac{\partial}{\partial x_j}(M_j D \bar{\mathcal{S}})$, the odd order field $\bar{X}^{\text{stat}}$ is computed from the stationary *Fick's law*

$$\bar{X}^{\text{stat}} = D\Big(-\sum_{j=1}^{3} \bar{M}_j \frac{\partial X^{\text{stat}}}{\partial x_j} + \bar{\mathcal{S}}\Big), \tag{29}$$

and finally the stationary delayed neutron precursor concentration is computed using Eq. (3).

We observe that, although the stationary state X^{stat}, $\bar{X}^{\text{stat}}$ should be a fixed point of the unperturbed Eqs. (27) and (26) in exact arithmetic, this does not need to be true in numerical computations with finite arithmetic. This point is illustrated in Section 3.1. The effect can be quantified if we rewrite, when the cross-sections do not change with time,

$$D^k_{\text{eff}} = [\bar{\Sigma}_a + (\nu\Delta t)^{-1}]^{-1} = [\bar{\Sigma}_a]^{-1}[1 + (\nu\Delta t\bar{\Sigma}_a)^{-1}]^{-1} \simeq D\left[1 + O((\nu\Delta t\,\bar{\Sigma}_a)^{-1})\right],$$

so for *small* values of the parameter $(\nu\Delta t\,\bar{\Sigma}_a)^{-1}$ Eqs. (26) and (29) are numerically equivalent, and then the diffusion matrix from the stationary Eq. (28) is, up to order $(\nu\Delta t\,\bar{\Sigma}_a)^{-1}$, equivalent to the time discretized Eq. (27). Some approximate numerical schemes in the literature assume that the odd order fields do not change (or change very little) with time, but this is not the case in this work.

2.4. Spatial discretization. The nodal collocation method

If we consider the diffusive nature of Eq. (27), a good candidate to the spatial discretization is a nodal collocation method. We will see that this method allows accurate results using a coarse spatial discretization, thus reducing computational time and memory storage. This method was initially developed for the neutron diffusion equation in [32], see also [42]. The generalization to P_L equations of arbitrary odd order L and multi-dimensional rectangular geometries was later done in [5, 6], where the method was exhaustively described. When a more detailed spatial representation is required, see [43] for transient analysis, using the adiabatic approximation, of the second order even-parity formulation of the transport equation, and handling unstructured meshes in any geometry.

In order to establish the notation that will be later used, we will proceed to describe shortly the main ideas of the method.

1. The core volume V is approximated by N adjacent rectangular nodes with coordinates $N^e = [x_{1,i_1}, x_{1,i_1+1}] \times [x_{2,i_2}, x_{2,i_2+1}] \times [x_{3,i_3}, x_{3,i_3+1}]$, where $e = 1, \ldots, N$ is the node index; x_{k,i_j} are the vertex indices, that describe an structured rectilinear mesh, in Cartesian coordinates.
2. The physical properties (cross-sections, etc.) are assumed to be constant on each spatial node N^e.
3. After scaling node N^e to the canonical cube $N_u^3 = [-\frac{1}{2}, \frac{1}{2}]^3$, using the change of variable $u_j = [x_j - \frac{1}{2}(x_{j,i_j} + x_{j,i_j+1})]/\Delta x_j^e$, with $\Delta x_j^e = x_{j,i_j+1} - x_{j,i_j}$, for each spatial coordinate, the spatial dependence is approximated by a finite expansion in terms of orthonormal Legendre polynomials $\mathcal{P}_k(u) = \sqrt{2k+1}\, P_k(2u)$, $-\frac{1}{2} < u < \frac{1}{2}$, that is, $\int_{-1/2}^{+1/2} \mathcal{P}_k(u)\, \mathcal{P}_r(u)\, du = \delta_{kr}$. So, in terms of the new variables,

$$X^e(\vec{u}) = \sum_{k_1,k_2,k_3=0}^{M} x^e_{k_1,k_2,k_3} \prod_{j=1}^{3} \mathcal{P}_{k_j}(u_j)\,, \tag{30}$$

   where M is the spatial expansion order, and analogous expressions for $\bar{X}^e$ and C_j^e.
4. The truncated series (30) is then inserted into Eqs. (25), (26) and (27), and integrated, using the orthonormality properties, with respect to the Legendre polynomials $\mathcal{P}_k(u)$, obtaining a linear system for the unknown coefficients $x^e_{k_1,k_2,k_3}$ of X^e, see [36, 6] for explicit computations.
5. Coupling between neighbouring nodes and with boundary conditions is performed by double derivative terms in Eq. (27) using interface conditions, see Eqs. (13) and Eqs. (18). No cross-derivative term appears when the ESP_L approximation is used.
6. First order derivative terms in Eqs. (26), (27) and (29) are computed directly; if, for example, we integrate the derivative with respect to the first coordinate and use the orthonormality properties of $\mathcal{P}_k(u)$,

$$\begin{aligned}\iiint_{N_u^3} \frac{1}{\Delta x_1^e} \frac{\partial X^e}{\partial u_1} \prod_{j=1}^{3} \mathcal{P}_{r_j}(u_j)\, du_j &= \frac{1}{\Delta x_1} \sum_{k_1=0}^{M} x^e_{k_1,r_2,r_3} \int_{-1/2}^{+1/2} \mathcal{P}'_{k_1}(u_1) \mathcal{P}_{r_1}(u_1)\, du_1 \\ &= \sum_{k_1=r_1+1}^{M} \sqrt{2k_1+1}\, \sqrt{2r_1+1}\, (1-(-1)^{k_1+r_1})\, x^e_{k_1,r_2,r_3}\,.\end{aligned}$$

7. The resulting linear system is described by a matrix that is large, sparse, real and non-symmetric, and the dimension depends on the number of spatial nodes N, the order M of the Legendre expansion (30) and the order L of the spherical harmonics approximation. This linear system will be solved with a direct method when the dimension of the problem is small, and with an iterative solver for large systems.

3. Numerical results

The time discretization method described in previous Section has been incorporated into the FORTRAN 90 code SHNC (Spherical Harmonics-Nodal Collocation), obtaining an extended version of the code, which we use to solve time-dependent transport problems. The first version of the SHNC code for stationary problems was developed by the authors in previous works and

validated with criticality problems [36, 6] and also with stationary internal and external source problems [37]. The code is able to solve the P_L approximation to the transport equation, for arbitrary odd order L, for arbitrary number of energy groups, for multidimensional space in general rectangular geometries and with isotropic and anisotropic scattering and sources. The spatial discretization via a nodal collocation method allows large spatial nodes of rectangular shape resulting into linear systems numerically well-behaved and with lower dimension than other methods, obtaining results with similar accuracy.

Due to the stiffness of the system of equations, the discretization of the time dependence uses an implicit and unconditionally stable scheme allowing large constant time steps, only limited by the desired accuracy. The number of delayed neutron groups is arbitrary, and we allow for changes in time of the physical properties of the materials like, for example, cross-sections.

In the next Subsections the code will be applied to several test cases, of increasing complexity, showing the capability of the method to deal with fast and thermal transients. The resulting linear systems will be solved, for small dimensions, using a direct method and, for large systems, with an iterative method that takes advantage of the sparsity of the associated matrix. In particular, the LU factorization performed by the `SuperLU` general purpose library was employed [44] as a direct method, and the biconjugate gradient stabilized method BCGSTAB, with incomplete LU factorization ILUT, from the `FORTRAN` library `SPARSKIT` [45], was used as iterative solver for medium to large systems. All calculations were carried out sequentially (single-core) on an AMD Phenom 2.8GHz computer. Only CPU times will be given for medium to large sized problems, where the performance of the method is studied.

3.1. Time dependent one-dimensional homogeneous slab with isotropic internal source

To validate the numerical method described above, we first consider an academic problem in one spatial dimension. First, we will describe its analytical solution. With this test an appropriate choice of physical parameters will show significant differences between the diffusive approximation (P_1) and the transport theory. See, for instance, the literature cited in [46] on analytical solutions of time-dependent transport equation.

This problem consists of an 1D homogeneous slab of length L with no scattering and fission, with an isotropic internal source S and vacuum boundary conditions, described by the following set of equations ($\mu = \cos\theta$, $0 \le \theta \le \pi$):

$$\begin{cases} \frac{1}{v}\frac{\partial \Phi}{\partial t} + \mu\frac{\partial \Phi}{\partial x} + \Sigma_t \Phi = S\,, \quad -\frac{L}{2} < x < +\frac{L}{2}\,,\ -1 < \mu < +1\,,\ t > 0\,, \\ \Phi(-\frac{L}{2}, \mu > 0, t) = 0\,, \quad \Phi(+\frac{L}{2}, \mu < 0, t) = 0\,, \quad t \ge 0\,, \\ \Phi(x, \mu, t = 0) = 0\,, \quad -\frac{L}{2} < x < +\frac{L}{2}\,,\ -1 < \mu < +1\,. \end{cases} \tag{31}$$

If we consider $\mu \neq 0$, the change of variable $\xi = x + \mu v t$, $\eta = x - \mu v t$, allows us to obtain the general solution of the equation

$$\Phi(\xi, \eta) = F(\eta) e^{-\frac{\Sigma_t}{2\mu}\xi} + \frac{S}{\Sigma_t}\,, \quad |\xi + \eta| < L\,,\ \frac{1}{\mu}(\xi - \eta) > 0\,,$$

with $F(\eta)$ an arbitrary function of η. Imposing the boundary and the initial conditions, the unique solution of (31), in the original variables, is

$$\Phi(x, \mu, t) = \begin{cases} \frac{S}{\Sigma_t}\left(1 - e^{-\frac{\Sigma_t}{\mu}(x + \frac{L}{2})}\right), & x - \mu v t < -\frac{L}{2}\,, \\ \frac{S}{\Sigma_t}\left(1 - e^{-\Sigma_t v t}\right), & -\frac{L}{2} < x - \mu v t < +\frac{L}{2}\,, \\ \frac{S}{\Sigma_t}\left(1 - e^{-\frac{\Sigma_t}{\mu}(x - \frac{L}{2})}\right), & x - \mu v t > +\frac{L}{2}\,. \end{cases} \tag{32}$$

From here the scalar flux can be computed as

$$\begin{aligned}\phi(x,t) &= \frac{1}{2}\int_{-1}^{+1}\Phi(x,\mu,t)\,d\mu \\ &= \frac{S}{\Sigma_t}\left[1-\frac{1}{2}\Big(e^{-\Sigma_t vt}(m_+ + m_-) + \int_{m_-}^{1} e^{-\frac{\Sigma_t}{\mu}(\frac{L}{2}-x)}d\mu + \int_{m_+}^{1} e^{-\frac{\Sigma_t}{\mu}(\frac{L}{2}+x)}d\mu\Big)\right], \\ &\qquad -\frac{L}{2} < x < +\frac{L}{2}\,,\ t>0\,, \quad (33)\end{aligned}$$

where $m_\pm = \min\left(\pm(x \pm L/2)/(vt), 1\right)$ (notice that $m_\pm \to 0$ when $t \to \infty$) and, finally, the stationary scalar flux is

$$\begin{aligned}\bar{\phi}(x) = \lim_{t\to\infty}\phi(x,t) &= \frac{S}{\Sigma_t}\Big[1-\int_0^1 e^{-\frac{\Sigma_t}{\mu}\frac{L}{2}}\cosh\Big(\frac{\Sigma_t}{\mu}x\Big)d\mu\Big] \\ &= \begin{cases}\frac{S}{\Sigma_t}\left[1-\frac{1}{2}(e^{-s_+}+e^{-s_-}-s_+E_1(s_+)-s_-E_1(s_-))\right], & -\frac{L}{2}<x<+\frac{L}{2}\,, \\ \frac{S}{2\Sigma_t}(1-e^{-s_0}+s_0E_1(s_0))\,, & x=\pm\frac{L}{2}\,,\end{cases} \quad (34)\end{aligned}$$

where $s_\pm = \Sigma_t(L/2 \pm x)$, $s_0 = \Sigma_t L$ and $E_1(z) = \int_z^\infty e^{-t}/t\,dt$ is the exponential integral function, that is defined for $|\arg(z)| < \pi$. Numerical evaluation of the integrals appearing in Eq. (33) was performed with `MATLAB`'s function `quad()`, using an adaptive Simpson's quadrature rule.

In the following we will perform a numerical analysis of the convergence of the P_L solutions for this problem with respect to the angular order and the temporal step size, while keeping constant the spatial discretization parameters, that is, the spatial mesh size $\Delta x = 0.1$ and the Legendre polynomial order $M = 4$ in Eq. (30). The effect of the spatial discretization and Legendre order on the convergence of the solutions will be analyzed for a 2D problem in Section 3.3.

A particular choice of the physical parameters that differentiates the diffusion solution from the transport solution is the following: $L = 1$, $\Sigma_t = S = 1$, $v = 10$, in adimensional units. The slab is then only 1 mean free path (Σ_t^{-1}) thick so we expect low accuracy from diffusion theory, specially near vacuum boundaries.

As commented in Section 1, due to the small dimension of the resulting linear systems, direct methods are fast (all calculations required less than 1 second of CPU time) and will be used in their resolution.

To investigate if the stationary state is preserved after the time discretization and its dependence with the parameter $(v\Delta t\,\Sigma_t)^{-1}$ (see comments at the end of Section 2.3) then, taking into account that $\Sigma_t = 1$, in Table 1 we compare the evolution of the stationary state, in the Euclidean norm, for different values of $(v\Delta t)^{-1}$, at different times, for the first P_L orders. In the Table, X is the even l vector introduced in Eqs. (22)-(24). At $t = 5$ the evolution has arrived to an stationary state, and we also observe in Table 1 that the relative difference from the initial state at each time t decreases linearly with $(v\Delta t)^{-1}$, and that values of the parameter $(v\Delta t)^{-1}$ in the range of the Table track the stationary state with good accuracy.

Taking into account these observations, we now study the convergence of the successive P_L approximations to Eq. (31), for particular values of the constant time step $\Delta t = 0.01$ and $\Delta t = 0.1$. In Table 2 we compare the relative error between the scalar flux of the exact solution, ϕ^{exact} from Eq. (33), and the approximate solution ϕ^k for different P_L orders. We can observe the typical convergence of the P_L approximations, that slows down for high order L, and that approximations of order higher than P_5 achieve minor improvements in accuracy.

Table 1: Comparison of the evolution of the P_1 and P_3 stationary state X^k at different times, with X^{stat}, for different constant time steps.

			$\|\|X^{\text{stat}} - X^k\|\|_2 / \|\|X^{\text{stat}}\|\|_2$				
	Δt	$(v\Delta t)^{-1}$	$t = 0.01$	$t = 0.1$	$t = 1.0$	$t = 2.0$	$t = 5.0$
	0.01	10	4.26E-5	1.13E-3	2.84E-3	2.84E-3	2.84E-3
P_1	0.1	1.0	–	9.67E-5	2.85E-4	2.85E-4	2.85E-4
	1.0	0.1	–	–	2.48E-5	2.82E-5	2.85E-5
	0.01	10	6.34E-5	1.63E-3	4.85E-3	4.85E-3	4.85E-3
P_3	0.1	1.0	–	1.50E-4	4.91E-4	4.91E-4	4.91E-4
	1.0	0.1	–	–	4.20E-5	4.83E-5	4.91E-5

Table 2: Relative error of successive P_L approximations to the scalar flux, for constant time steps Δt.

		$\|\|\phi^{\text{exact}} - \phi^k\|\|_2 / \|\|\phi^{\text{exact}}\|\|_2$				
Δt	t	P_1	P_3	P_5	P_7	P_9
	0.01	7.57E-2	7.04E-2	6.98E-2	6.96E-2	6.96E-2
	0.02	6.87E-2	6.28E-2	6.24E-2	6.23E-2	6.23E-2
	0.03	6.46E-2	5.82E-2	5.77E-2	5.75E-2	5.75E-2
0.01	0.05	6.02E-2	5.20E-2	5.11E-2	5.08E-2	5.06E-2
	0.10	5.63E-2	3.70E-2	3.23E-2	3.08E-2	3.02E-2
	1.00	9.45E-2	1.97E-2	9.62E-3	8.36E-3	7.23E-3
	5.00	9.45E-2	1.97E-2	9.62E-3	8.36E-3	7.23E-3
	0.10	2.61E-1	2.39E-1	2.37E-1	2.37E-1	2.36E-1
	0.20	1.52E-1	1.11E-1	1.06E-1	1.05E-1	1.04E-1
0.1	0.30	1.12E-1	5.56E-2	4.83E-2	4.61E-2	4.50E-2
	0.50	9.77E-2	2.69E-2	1.66E-2	1.38E-2	1.17E-2
	5.00	9.67E-2	2.30E-2	1.15E-2	8.86E-3	7.00E-3

Finally, Fig. 1 shows the P_1 and P_3 approximations to the scalar flux ϕ in different times, together with the exact solution for this problem, when the time step is set to $\Delta t = 0.01$. We observe that P_3 solution gives a better approximation than P_1 solution.

3.2. One-dimensional subcritical transient benchmark with two energy groups

The one-dimensional reactor benchmark [47, BSS-6] consists of three zones with physical data given in Table 3 and with geometry shown in Fig. 2. We have computed the total cross-section from the diffusion coefficient taken as $D_g = (3\Sigma_{t,g})^{-1}$ for energy group index $g = 1, 2$. However, notice that in Eqs. (10) and (11) only appear absorption cross-sections. This case consists of a two energy groups and six delayed-neutron groups problem, that is well described by the diffusion approximation, as computed in [47]. We have omitted in Table 3 the delayed neutron emission spectrum, that is equal to the fission spectrum for prompt neutrons. At reactor boundaries the flux is set to zero. The initial state is set to the critical state, that is previously computed for each P_L approximation. That means that the fission cross-sections in Table 3 are divided by the k_{eff} eigenvalue from the criticality calculation of the corresponding P_L approximation [5]; see Table 4 where the k_{eff} eigenvalue computed in [47] is taken as reference. The initial precursor concentrations are obtained from the stationary equation (3) and the initial critical flux distribution.

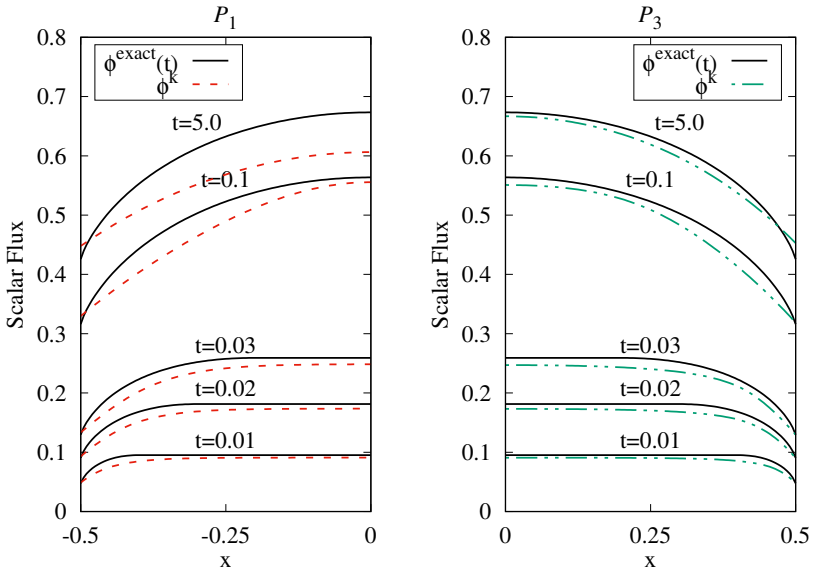

Figure 1: Comparison of P_1 (left) and P_3 (right) approximations to the scalar flux, ϕ^k (discontinuous line), with the exact solution ϕ^{exact} (continuous line), for constant time step $\Delta t = 0.01$.

Table 3: Physical properties of the one-dimensional transient benchmark. The delayed neutron emission spectrum is equal to the fission spectrum. Cross-sections are in cm^{-1}, lengths in cm and times in seconds.

Material	Group g	$\Sigma_{a,g}$	$\Sigma_{t,g}$	$\chi_{p,g}$	$\nu\Sigma_{f,g}$	$\Sigma_{s,g\to1}$	$\Sigma_{s,g\to2}$	v_g
1 and 3	1	0.026	0.22222	1	0.010	0.19622	0.01500	10^7
	2	0.180	0.66667	0	0.200	0.00000	0.48667	$3 \cdot 10^5$
2	1	0.020	0.33333	1	0.005	0.31333	0.01000	10^7
	2	0.080	0.66667	0	0.099	0.00000	0.58667	$3 \cdot 10^5$

	Delayed neutron parameters					
Type	1	2	3	4	5	6
β_j	0.00025	0.00164	0.00147	0.00296	0.00086	0.00032
λ_j	0.01240	0.03050	0.11100	0.30100	1.04000	3.01000

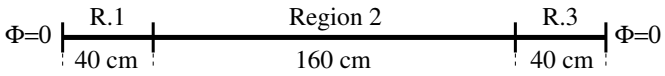

Figure 2: Geometrical configuration of the 1D subcritical transient benchmark.

Table 4: Computed k_{eff} eigenvalue for successive P_L approximations and reference value, for the 1D benchmark.

	P_1	P_3	P_5	Reference
k_{eff}	0.9015978	0.9024870	0.9025005	0.9015507

The initial equilibrium state is then perturbed from $t = 0\,\text{s}$ to $t = 1\,\text{s}$ by increasing the absorption cross-section for energy group 2 in Region 1 by 3%, and the simulation ends at $t = 2\,\text{s}$,

that corresponds to the following decrease in the scattering cross-section:

$$\Sigma^1_{s,2\to 2}(t) = \begin{cases} 0.48667 - 0.18 \cdot 0.03\, t\,, & 0\,\mathrm{s} \le t \le 1\,\mathrm{s}\,, \\ 0.48127\,, & t > 1\,\mathrm{s}\,. \end{cases}$$

We will compare our results with the diffusive computations in [47], so we consider the same spatial mesh size $\Delta x = 2\,\mathrm{cm}$ and two choices for the time step: $\Delta t = 10^{-1}\,\mathrm{s}$ and $\Delta t = 10^{-2}\,\mathrm{s}$. Notice that these choices give the parameter $\max_{g=1,2}(v_g\,\Delta t\,\Sigma_{t,g})^{-1} \le 5 \cdot 10^{-5}$ for $\Delta t = 10^{-1}\,\mathrm{s}$, and $\le 5 \cdot 10^{-4}$ for $\Delta t = 10^{-2}\,\mathrm{s}$.

Table 5 shows the total power of the successive P_L approximations, normalized such that the initial ($t = 0\,\mathrm{s}$) power is the unity, for both time steps. It is seen that high order P_L approximations alter the third significant digit in the diffusive P_1 computation. The same change in the results can be observed when the time step size is decreased, keeping the same angular order L of the P_L approximation.

Table 5: Total power relative to the initial power computed for successive P_L approximations and for different constant time steps Δt. Last column shows the reference (diffusive) values.

	$\Delta t = 10^{-1}$ s			$\Delta t = 10^{-2}$ s			
t (s)	P_1	P_3	P_5	P_1	P_3	P_5	Reference
0.0	1.0000	1.0000	1.0000	1.0000	1.0000	1.0000	1.0000
0.1	0.9270	0.9262	0.9262	0.9277	0.9269	0.9269	0.9298
0.2	0.8685	0.8673	0.8673	0.8696	0.8685	0.8685	0.8732
0.5	0.7520	0.7506	0.7506	0.7534	0.7519	0.7520	0.7596
1.0	0.6497	0.6488	0.6488	0.6517	0.6507	0.6508	0.6588
1.5	0.6350	0.6342	0.6342	0.6367	0.6359	0.6359	0.6432
2.0	0.6229	0.6223	0.6223	0.6245	0.6239	0.6239	0.6306

Table 6 shows a comparison of the relative power fractions for each region, between the P_5 approximation and the reference diffusive calculation, both for a constant time step $\Delta t = 10^{-1}\,\mathrm{s}$. Also, Fig. 3 and Fig. 4 show, respectively, the scalar flux (fast and thermal) and the power distribution, for the same time step, using the P_5 approximation, and for different times. We have also computed the scalar flux ϕ using smaller time step $\Delta t = 10^{-2}\,\mathrm{s}$ and verified that, for all P_L approximations, $L = 1, 3, 5$, the magnitude of the relative error with respect to the solution with $\Delta t = 10^{-1}\,\mathrm{s}$ is about 10^{-3}.

Table 6: Relative power fractions, normalized to unit initial power, for each region, when $\Delta t = 10^{-1}\,\mathrm{s}$, for P_5 approximation and reference values.

	P_5			Reference		
t (s)	Reg.1	Reg. 2	Reg. 3	Reg. 1	Reg. 2	Reg. 3
0.0	1.0000	1.0000	1.0000	1.0000	1.0000	1.0000
0.1	0.8589	0.9324	0.9910	0.8621	0.9339	0.9910
0.2	0.7472	0.8780	0.9832	0.7520	0.8804	0.9830
0.5	0.5277	0.7695	0.9662	0.5336	0.7724	0.9655
1.0	0.3405	0.6732	0.9477	0.3452	0.6753	0.9462
1.5	0.3194	0.6572	0.9401	0.3235	0.6587	0.9381
2.0	0.3027	0.6443	0.9334	0.3066	0.6455	0.9311

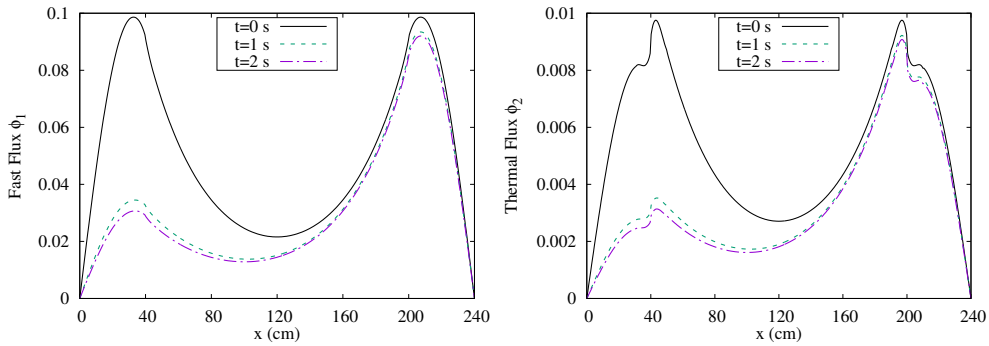

Figure 3: P_5 fast (left) and thermal (right) scalar fluxes ($\Delta t = 10^{-1}$ s).

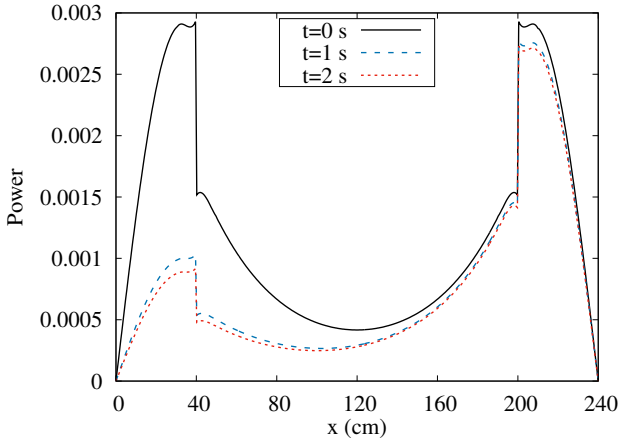

Figure 4: P_5 power distribution ($\Delta t = 10^{-1}$ s).

3.3. Two-dimensional TWIGL reactor problem

We use the numerical methods to model two transients of the TWIGL benchmark problem. It was originally proposed by [48] and later has been studied with different methods (see, for instance, [49] for a compilation of results, mostly based on the diffusion approximation, see also [50]), then the numerical results shown in this work can be compared with solutions obtained by previous methods and codes.

This benchmark is a two-dimensional reactor core with two energy group cross-sections using one delayed neutron precursor family. The TWIGL core configuration consists of three fuel material regions with no reflector region. Materials 1 and 2 are seed regions and material 3 in central and outer regions is blanket.

Fig. 5 shows geometry and dimensions of the quarter reactor and Table 7 provides the material cross-sections and the kinetic parameters. The delayed neutron emission spectrum is equal to the fission spectrum. Zero flux boundary conditions are considered at the external surfaces.

The material properties of regions 1 and 2 are the same, but two different transients are simulated in region 1 with control rod insertion. Each transient is modeled by varying the thermal absorption cross-section $\Sigma_{a,2}$ with different speed.

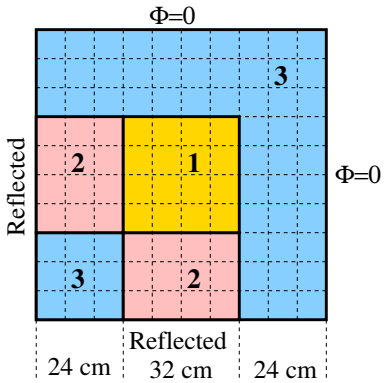

Figure 5: Geometrical configuration of the 2D TWIGL benchmark.

Table 7: Physical properties for TWIGL problem. Cross-sections are in cm^{-1}, lengths in cm and times in seconds.

Material	Group g	$\Sigma_{a,g}$	$\Sigma_{t,g}$	$\chi_{p,g}$	$\nu\Sigma_{f,g}$	$\Sigma_{s,g\to1}$	$\Sigma_{s,g\to2}$	v_g
1 and 2	1	0.01	0.238095	1	0.007	0.218095	0.01	10^7
	2	0.15	0.83333	0	0.2	0.0	0.68333	$2\cdot10^5$
3	1	0.008	0.25641	1	0.003	0.23841	0.01	10^7
	2	0.05	0.66667	0	0.06	0.0	0.61667	$2\cdot10^5$
Delayed neutron parameters:		$\beta = 0.0075$, $\lambda = 0.08$.						

The initial condition for the transients is a steady-state distribution and the system is initially made critical by dividing the fission cross-section by the eigenvalue k_{eff}. Computed P_L ($L = 1, 3, 5$) and ESP_3 solutions of k_{eff} are given in Table 8, obtained using a discretization mesh with 10×10 nodes for the quarter reactor ($\Delta x = \Delta y = 8\,\text{cm}$, see Fig. 5) and order $M = 4$ in the Legendre expansion (30). The Table also shows the eigenvalue solution of QUANDRY [51], obtained with diffusive computations with the same node size.

Table 8: TWIGL eigenvalue k_{eff} for initial condition, calculated with successive P_L and ESP_3 approximations, and QUANDRY solution.

	P_1	P_3	P_5	ESP_3	QUANDRY
k_{eff}	0.9132077	0.9137538	0.9137628	0.9135600	0.91321

3.3.1. Transient 1: Linear ramp reactivity perturbation

In the first transient considered, the initial state is perturbed from $t = 0$ s to $t = 0.2$ s by linearly decreasing the absorption cross-section of Region 1 for energy group 2, from 0.15 cm^{-1} to 0.1465 cm^{-1}. The total time for the transient is 0.5 s, then it corresponds to the following increase in the scattering cross section:

$$\Sigma^1_{s,2\to2}(t) = \begin{cases} 0.68333 + 0.11667 \cdot 0.15\,t\,, & 0\,\text{s} \le t \le 0.2\,\text{s}\,, \\ 0.68683\,, & t > 0.2\,\text{s}\,. \end{cases}$$

TWIGL ramp perturbation is used in this work to study the sensitivity of the numerical model. As a starting point, we study the convergence of the P_1 solutions when the temporal step size changes. The results are shown in Table 9. Computational efficiency is also analyzed when the temporal mesh changes, by comparing CPU times in the Table (in seconds). The spatial mesh considered is $\Delta x = \Delta y = 8$ cm, which is one of the discretization options used in reference works, and the order of Legendre polynomials considered is $M = 4$.

Table 9: Comparison of the numerical SHNC P_1 relative power when varying the temporal step size for TWIGL ramp perturbation, and CPU times ($\Delta x = \Delta y = 8$ cm).

Δt	2.5 ms	5 ms	10 ms	20 ms	50 ms
Time (s)	Relative power				
0.0	1.0000	1.0000	1.0000	1.0000	1.0000
0.1	1.3094	1.3110	1.3122	1.3136	1.3167
0.2	1.9651	1.9693	1.9731	1.9785	1.9916
0.3	2.0787	2.0824	2.0845	2.0860	2.0874
0.4	2.0959	2.0998	2.1020	2.1039	2.1072
0.5	2.1134	2.1173	2.1196	2.1215	2.1249
CPU time (s)	22	11	6	3	2

We observe that, taking the column with smallest time step $\Delta t = 2.5$ ms as reference, the absolute error decreases (at least) linearly with the time step size, in agreement with the accuracy of the implicit Euler method.

Setting the time step size to $\Delta t = 2.5$ ms and considering spatial discretization with nodes of side length 8 cm, we have calculated the solutions for this problem by varying the angular order L of the P_L approximation, and also with the ESP_3 approximation. In Table 10 we display these results for the relative power, comparing them with solutions of QUANDRY [51] and S_4 [52]. QUANDRY results were obtained with diffusive calculations using transient convergence criterion 10^{-3} and S_4 corresponds to the solution of the transport time-dependent equation using a discrete ordinates method; for more details see references [51, 52]. The Table specifies the spatial discretization and the time step size used by each method.

In order to estimate how fast is each simulation, we also tabulate the execution time needed in each P_L and ESP_3 calculation. As the time depends on the characteristics of the computer, the desired accuracy, etc., we omit the CPU times of other references in Table 10, which can be consulted in the literature. For the numerical computation of the P_L solutions, when the size of the problem is small (P_1) we use a direct method (LU factorization) and when the dimension grows (P_3, ESP_3, P_5), an iterative method (BCGSTAB/ILUT) with tolerance 10^{-12} is used.

We observe in Table 10 that the P_3 approximation, with the present level of spatial and temporal error, is sufficient to obtain P_L converged results for this transient of TWIGL benchmark. We do not observe differences between the P_5 and the P_3 solutions up to the fifth or sixth significant digit. Also, ESP_3 approximation shows good agreement with the reference values with less computational time and computer storage than the corresponding P_3 approximation. The CPU time needed in ESP_3 calculations for this problem is about 16% smaller than the time required for the P_3 approximation, because in this approximation we keep the number of components of vector X and only reduce the number of nonzero elements of the sparse matrix of the linear system.

There is good agreement in Table 10 between the results of QUANDRY, obtained with diffu-

Table 10: Relative power, normalized to unit initial power, for P_L and ESP_3 approximations in comparison with other methods, for TWIGL ramp perturbation.

Method	P_1	P_3	P_5	ESP_3	QUANDRY	S_4
Mesh		10×10			10×10	10×10
Δt (ms)		2.5			2.5	0.1
Time (s)	Relative power					
0.0	1.0000	1.0000	1.0000	1.0000	1.000	1.000
0.1	1.3094	1.3115	1.3116	1.3124	1.307	1.312
0.2	1.9651	1.9746	1.9746	1.9781	1.955	1.975
0.3	2.0787	2.0900	2.0900	2.0944	2.075	2.097
0.4	2.0959	2.1075	2.1076	2.1121	2.092	2.115
0.5	2.1134	2.1252	2.1253	2.1299	2.110	2.133
CPU time (s)	22	569	2298	477	–	–

sive calculations, and the P_1 solutions. Also, it can be seen how the P_5 results are closer to the S_4 solution.

We have studied the impact on the solutions of varying the spatial discretization and the order of Legendre polynomials M considered in Eq. (30). Table 11 displays the P_3 results of the relative power for different mesh size and for different order M, when the time step size is fixed to $\Delta t = 2.5$ ms. The first mesh is non uniform, 3×3, and partitions each direction x, y into 3 subintervals of length 24, 32 and 24 cm, that corresponds to one rectangular node per material. The second non uniform mesh, 6×6, halves the previous intervals, then the size subintervals are 12, 16 and 12 cm. The other meshes, 10×10 and 20×20, correspond to square nodes with side length 8 cm and 4 cm, respectively.

Table 11: Comparison of the numerical SHNC P_3 relative power when varying the mesh size and the order M, for TWIGL ramp perturbation, and CPU times ($\Delta t = 2.5$ ms).

Mesh	3×3		6×6		10×10		20×20	
Order M	3	4	3	4	3	4	3	4
Time (s)	Relative power							
0.0	1.0000	1.0000	1.0000	1.0000	1.0000	1.0000	1.0000	1.0000
0.1	1.3102	1.3102	1.3098	1.3092	1.3115	1.3115	1.3127	1.3130
0.2	1.9683	1.9708	1.9702	1.9696	1.9745	1.9746	1.9772	1.9777
0.3	2.0831	2.0858	2.0850	2.0841	2.0899	2.0899	2.0931	2.0937
0.4	2.1005	2.1033	2.1024	2.1016	2.1075	2.1075	2.1108	2.1113
0.5	2.1180	2.1209	2.1200	2.1191	2.1252	2.1252	2.1285	2.1291
CPU time (s)	6	16	36	130	147	568	1228	5296

As can be seen from Table 11, P_L solutions can be calculated considering a spatial discretization mesh with large nodes, obtaining reasonably accurate results, with considerable saving in computational cost. We observe that, in calculations with large spatial nodes, the results are more sensitive to changes in the Legendre order M. When nodes with side length of 8 cm or more are considered, convergent results are obtained without the need to take a high order M.

3.3.2. *Transient 2: Step reactivity perturbation*

In the second transient, a step change is considered in the thermal absorption cross-section of Region 1, by reducing its value from 0.15 cm^{-1} to 0.1465 cm^{-1}. Then the corresponding scattering cross-section increases to $\Sigma^1_{s,2\to 2}(t) = 0.68683\ cm^{-1}$, for $0\,s \le t \le 0.5\,s$.

Taking into account the analysis made for the ramp perturbation of TWIGL, we apply now the values $\Delta t = 2.5\,ms$ and $\Delta x = \Delta y = 8\,cm$ as time step and mesh step sizes respectively, because for these values it is possible to obtain convergent solutions. In Table 12 we display the P_1, P_3 and ESP_3 relative power solutions for this transient, together with results of QUANDRY [51] and S_4 [52]. We omit in the Table the P_5 solutions because, as commented in the previous transient, the differences between P_5 and P_3 solutions are very small for this problem.

Table 12: Relative power, normalized to unit initial power, for P_1, P_3 and ESP_3 approximations in comparison with other methods, for TWIGL step perturbation.

Method	P_1	P_3	ESP_3	QUANDRY	S_4
Mesh		10×10		10×10	10×10
Δt (ms)		2.5		2.5	0.1
Time (s)	Relative power				
0.0	1.0000	1.0000	1.0000	1.000	1.000
0.1	2.0654	2.0765	2.0808	2.061	2.083
0.2	2.0827	2.0941	2.0985	2.078	2.101
0.3	2.1000	2.1117	2.1162	2.095	2.119
0.4	2.1175	2.1294	2.1341	2.113	2.137
0.5	2.1351	2.1473	2.1521	2.131	2.155

Finally, Fig. 6 shows the normalized relative power for both transients: ramp and step perturbations. The Figure compares the P_1, P_3 and P_5 results with the QUANDRY and S_4 solutions. The choice of the spatial mesh and time discretization is the same as the one considered in Tables 10 and 12.

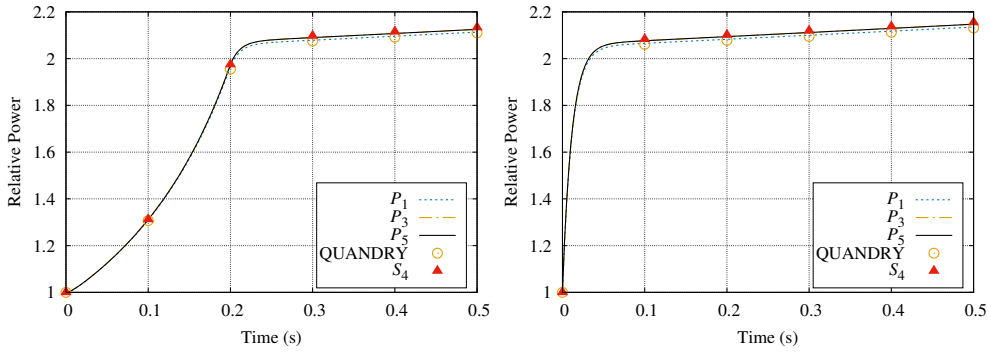

Figure 6: Relative power for TWIGL problem. Left: Linear ramp perturbation. Right: step perturbation.

3.4. *C5 MOX transient benchmark*

For the validation of the numerical method applied to reactors with more complex geometry and configuration, we study in this Section a two-dimensional two-group C5 MOX time-

dependent benchmark. This problem is based on the steady-state C5 MOX problem studied originally by the authors in a previous work [53], which was a variant of the C5 MOX fuel assembly problem described in [54]. From the steady-state solution (Fig. 10) we observe that a precise description of the strong spatial gradients in the neutron flux requires high order P_L methods and, as we will see, the same is true when we track the time evolution of the neutron flux at the pin level.

As can be seen in Fig. 7, the core configuration of the C5 MOX benchmark consists of 16 squared fuel assemblies, 8 of type UO_2 and 8 of type MOX (mixed oxide fuel assemblies). The side of each assembly is 21.42 cm length and the total size of the reactor is 128.52 cm×128.52 cm. The core is surrounded by a reflector region and vacuum conditions are applied at the external boundaries.

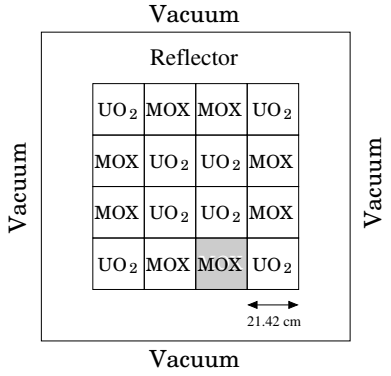

Figure 7: 2D configuration for the C5 MOX benchmark. The transient is carried out at the shaded assembly.

Each MOX and UO_2 assembly is structured in 17×17 squared pin cells of side length 1.26 cm, see Fig. 8; 264 of them are homogenized fuel pins, 24 are guide tube (GT) and one is a centered tube for fission chamber (FC). From the Figure we see that each MOX assembly has fuel pins with three different enrichments.

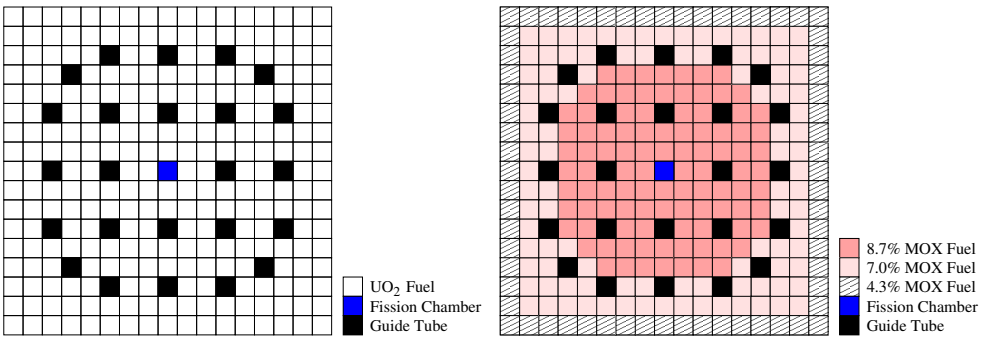

Figure 8: Geometry of UO_2 (left) and MOX (right) assemblies and pin cell compositions.

The two-group cross-sections for all types of pin cells (three enrichments of MOX, UO_2, GT and FC) and the reflector are provided in Table 13.

Table 13: Cross-sections (cm^{-1}) and velocities (cm/s) for the 2D C5 MOX benchmark. Energy groups 1 and 2 correspond to the fast and thermal energy group, respectively.

pin cell type	Group g	$\Sigma_{t,g}$	$\nu\Sigma_{f,g}$	$\Sigma_{s,g\to1}$	$\Sigma_{s,g\to2}$	v_g
4.3% MOX fuel	1	0.550	0.0075	0.520	0.015	1.22628E+7
	2	1.100	0.300	0.0	0.90	2.88714E+5
7.0% MOX fuel	1	0.550	0.0075	0.520	0.015	1.46202E+7
	2	1.01	0.375	0.0	0.76	2.92249E+5
8.7% MOX fuel	1	0.550	0.0075	0.520	0.015	1.59499E+7
	2	1.060	0.450	0.0	0.760	2.93512E+5
UO_2 fuel	1	0.570	0.005	0.540	0.020	7.73247E+6
	2	1.100	0.125	0.0	1.00	2.87886E+5
Guide Tube	1	0.586	0.000	0.560	0.025	7.68974E+5
	2	1.220	0.000	0.0	1.20	2.88616E+5
Reflector	1	0.611	0.000	0.560	0.050	7.73247E+6
	2	2.340	0.000	0.0	2.300	2.87886E+5
Fission Chamber	1	0.586	10^{-7}	0.560	0.025	8.73088E+5
	2	1.220	$3\cdot10^{-6}$	0.0	1.20	2.62899E+5

The two energy groups velocities for each pin cell, given in Table 13, have been generated from the C5G7 benchmark [55] using the standard volume weighting method [56] for pin cell spatial homogenization and energy group collapse. In particular, energy group 1 comes from C5G7 fast energy groups $1-6$ and energy group 2 from C5G7 thermal group 7. For each distinct pin cell:

1. The physical parameters of the C5G7 benchmark are used to compute the P_3 solution, Φ_g, $g = 1,\dots,7$, of an isolated pin cell, with reflecting boundary conditions, and spatial mesh given by a 7×7 nodes as described in Fig. 4 of [57].
2. The averaged velocity for each collapsed energy group g' is then computed from the flux volume weighted formula

$$\frac{1}{v_{g'}} = \frac{\int_V dV \sum_{g\in I_{g'}} \frac{1}{v_g}\Phi_g}{\int_V dV \sum_{g\in I_{g'}} \Phi_g}\,, \quad g' = 1,2\,,$$

   where V is the pin cell volume and $I_{g'}$ is the interval of energy groups that collapse to energy group g', that is, $I_1 = \{1-6\}$ and $I_2 = \{7\}$.

The model, finally, includes eight families of delayed neutron groups with the same physical parameters specifications given in [55], except for the neutron spectrum that is collapsed to two energy groups as $\chi_{d,jg'} = \delta_{g'1}$, $g' = 1,2$, for $j = 1,\dots,8$.

The C5 MOX transient is carried out by replacing the material in the guide tubes with the reflector, in the MOX assembly at the left center of the south-east quarter reactor (see the shaded assembly in Fig. 7). This transient is modeled by a step change of the cross-sections in the GT pin cells, that simulates an instantaneous insertion of the reflector material, beginning from $t = 0\,\mathrm{s}$. The reflector stays until the end of the simulation, $t = 0.05\,\mathrm{s}$.

The transient is initiated with the critical condition made by dividing the fission cross-sections by the eigenvalue k_{eff}, previously calculated from the corresponding eigenvalue problem. P_L ($L = 1, 3$) and ESP_3 solutions of k_{eff} obtained with the SHNC code, together with diffusive and SP_3 k_{eff} values from the implementation in the numerical code PARCS [33], are given in Table 14. SHNC results of k_{eff} can be compared with the ones obtained in a previous work, using the serendipity approximation [53]. The P_L and ESP_3 solutions presented in this Section have been calculated using a discretization mesh with 102×102 squared nodes, that corresponds to a node for each pin cell ($\Delta x = \Delta y = 1.26\,\mathrm{cm}$) and order $M = 4$ in the Legendre expansion.

Table 14: C5 MOX eigenvalue k_{eff}, calculated with P_L and ESP_3 approximations and results from PARCS code.

Method	SHNC			PARCS	
	P_1	P_3	ESP_3	Diff	SP_3
k_{eff}	0.971429	0.970876	0.970879	0.971187	0.970542

To describe the complexity of the problem, Table 15 shows some computationally relevant parameters: the number of unknowns per spatial node, computed as $N^{\mathrm{node}} = N^{\mathrm{even}} \times G \times M^d$ where N^{even} is the number of elements in vector X for P_L approximation, G is the number of energy groups, M is the order of the spatial expansion in Legendre polynomials and d is the spatial dimension; the dimension n of the resulting sparse matrix obtained from the discretization of the implicit problem (27), and computed as the product of the number of spatial nodes, $(17 \times 6)^2$, by N^{node}; and the number of nonzero elements nnz of the sparse matrix.

Table 15: Computational parameters of the C5 MOX benchmark for P_L approximations, $L = 1, 3, 5$, and spatial Legendre order $M = 4$.

Approx.	N^{node}	n	nnz
P_1	$1 \times 2 \times 4^2 = 32$	332028	7235280
P_3	$4 \times 2 \times 4^2 = 128$	1331712	73717886
P_5	$9 \times 2 \times 4^2 = 288$	2996352	260529260

In Table 16 we display the relative power in the MOX assembly where the GT are replaced by reflector, at different time values, obtained with time step sizes $\Delta t = 0.1\,\mathrm{ms}$ and $\Delta t = 0.5\,\mathrm{ms}$, for different calculations. For brevity we have omitted P_5 results because there is not further improvement. As can be seen in the Table, the transient causes at $t = 0.05\,\mathrm{s}$ an increase of more than 50% the initial power value.

Table 17 shows the computed total relative power, when the time step is kept to 0.1 ms, and the Table also displays a comparison of the computation CPU times between the different calculations.

In P_3 calculations with time step $\Delta t = 0.5\,\mathrm{ms}$, the CPU time is reduced in about 36% with respect to the computation with $\Delta t = 0.1\,\mathrm{ms}$ and reductions of 64% and 58% are obtained in the P_1 and ESP_3 calculations, respectively.

Table 16: MOX assembly power, normalized to unit initial power, obtained with different methods.

Method	SHNC						PARCS
	P_1		P_3		ESP_3		SP_3
Δt (ms)	0.1	0.5	0.1	0.5	0.1	0.5	0.1
Time (s)	Assembly Power						
0.000	1.00000	1.00000	1.00000	1.00000	1.00000	1.00000	1.00000
0.001	1.25180	1.24499	1.23649	1.22825	1.18231	1.17220	1.24206
0.002	1.30797	1.31099	1.28355	1.28414	1.21300	1.20812	1.29703
0.005	1.41717	1.42893	1.37078	1.37766	1.26739	1.26425	1.40616
0.010	1.52397	1.54437	1.45327	1.46556	1.31639	1.31411	1.50677
0.020	1.60817	1.63903	1.51497	1.53375	1.35014	1.34957	1.57786
0.050	1.64443	1.68229	1.53951	1.56228	1.36211	1.36261	1.60447

Table 17: Total relative power for C5 MOX benchmark (Δt = 0.1 ms), and CPU times.

Method	SHNC			PARCS	
	P_1	P_3	ESP_3	Diff	SP_3
Time (s)	Total power				
0.000	1.00000	1.00000	1.00000	1.00000	1.00000
0.001	1.04981	1.04133	1.02872	1.05651	1.05164
0.002	1.08841	1.07268	1.04947	1.10116	1.09221
0.005	1.17767	1.14405	1.09556	1.20199	1.18305
0.010	1.26618	1.21269	1.13783	1.29713	1.26727
0.020	1.33593	1.26402	1.16697	1.36611	1.32679
0.050	1.36586	1.28433	1.17722	1.39197	1.34898
CPU times (h)	0.7	30	27	0.30	0.33

Fig. 9 shows the P_1, P_3, ESP_3 and PARCS results for MOX assembly power (left) and the total relative power (right) versus time for this transient process. We observe that, in both cases, the power steeply changes increasing, until the increase becomes smoother and for $t > 0.04$ s keeps its value almost constant. The increase of the total relative power is lower than that in the MOX assembly and we observe a sharp increase of the MOX assembly power at lower times. Also, it can be seen in the Figure that the power value is overestimated or underestimated by SP_3 and ESP_3 approximations. The SP_3 approximation improves the P_1 results, more than the ESP_3 method. For this kind of problems with sharp changes in the spatial flux distribution the importance of the neglected terms (couplings between orthogonal directions) in the ESP_3 approximation, and to a lesser extent in the SP_3 approximation, accumulates when time evolves, and only a full P_3 approximation gives precise results.

Fig 10 shows the P_1, P_3 and ESP_3 thermal scalar fluxes at $t = 0$ s and $t = 0.05$ s, along the line $y = 32.13$ cm that passes through the center of the MOX assembly, and for $64.26 \leq x \leq 128.52$ cm, that corresponds to the half-right reactor. Although the relative differences between the P_1 and P_3 MOX assembly relative power grow almost linearly with time from 1.2% to 6.8% (see Table 16, Δt = 0.1 ms), the differences in the pin-by-pin thermal flux are larger, and also grow with time. The first maximum in Fig. 10, is reached at the first pin cell center (x = 67.41 cm), where the thermal flux calculated with P_3 approximation increases from $4.038 \cdot 10^{-4}$

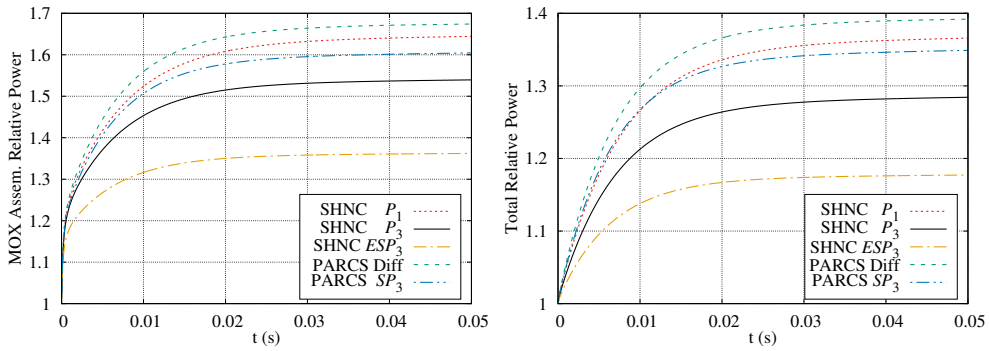

Figure 9: MOX assembly relative power (left) and total relative power (right) for C5 MOX transient benchmark, computed with different approximations.

at $t = 0\,\text{s}$ to $8.857 \cdot 10^{-4}$ at $t = 0.05\,\text{s}$. Large differences between P_1 and P_3 are observed at the pin cell centers. At $t = 0.05\,\text{s}$ these differences generally increase where space gradients are high: dips and peaks of MOX and UO_2 assemblies.

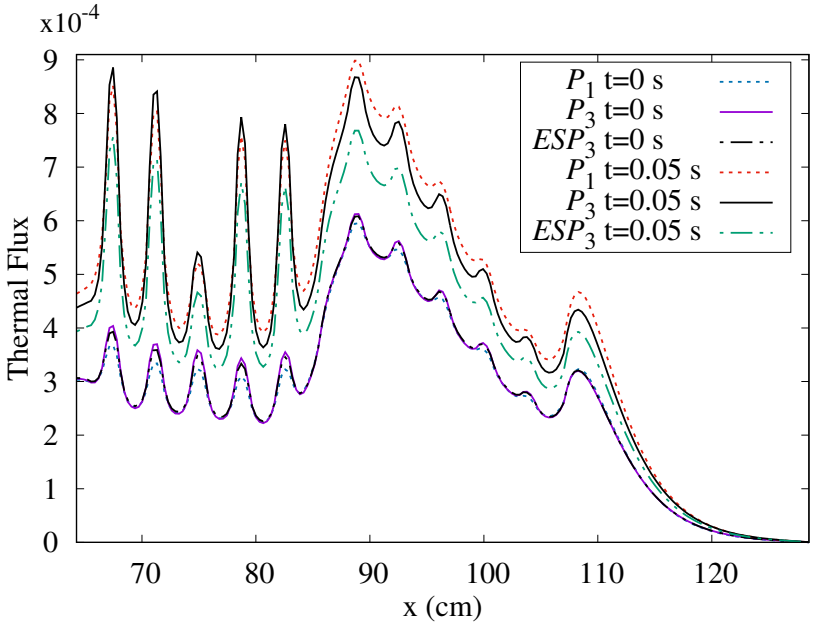

Figure 10: Thermal scalar flux along the line $y = 32.13$ cm for $t = 0$ s and $t = 0.05$ s, computed with P_1, P_3 and ESP_3 approximations.

Finally, Fig. 11 shows the P_3 scalar flux distribution at the core for the thermal ($g = 2$) energy group, at the initial time and at $t = 0.05\,\text{s}$. We observe the maximum value of the flux in the central UO_2 assemblies at $t = 0.05\,\text{s}$, and also an increase of the flux distribution is observed in the MOX assembly with the replaced GT by reflector.

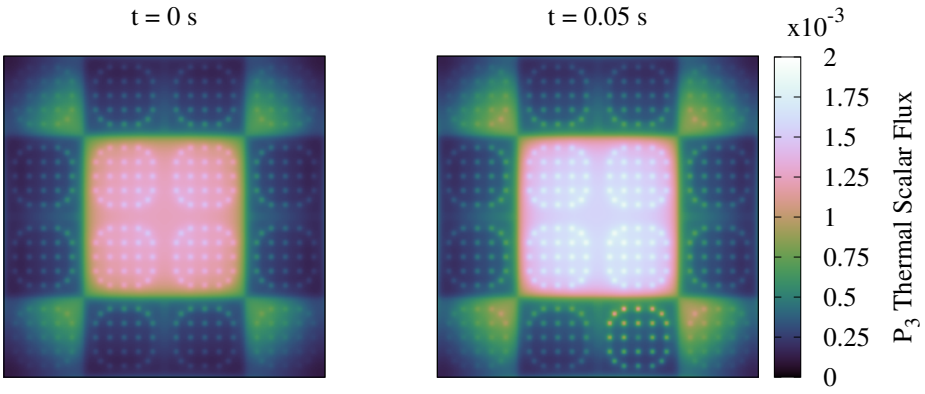

Figure 11: P_3 thermal flux distribution for $21.42 \leq x, y \leq 107.10$ cm. Left: steady-state. Right: $t = 0.05$ s.

4. Conclusions

We have developed in this work a method to solve the P_L spherical harmonics approximation to the time-dependent neutron transport equation. The numerical scheme is based on a first order finite difference implicit method for the time discretization of the equations and a nodal collocation method for the spatial discretization. This approach allows a reduction by half of the number of unknowns, the use of large time steps while keeping the numerical stability of the method, and finally the use of large spatial nodes with reasonable accuracy, leading to linear algebraic problems with moderate size and numerically well-behaved. The code allows arbitrary number of energy groups, of neutron precursor families and arbitrary P_L approximation, for odd L, and is able to deal with internal and external anisotropic sources, with anisotropic scattering.

Its computer implementation has been validated first against different time-dependent benchmark problems in 1D and 2D that show the convergence and accuracy of the method. Finally, a more realistic 2D problem with complex fuel geometry has been proposed showing that for precise results a high order P_L approximation is required, improving the diffusion and the SP_L approximations, and also a simple implementation of this last one based on removing cross-derivative terms from the full P_L equations. These approximations give accurate results for near diffusive problems, but for problems with strong spatial gradients the differences accumulate with time. Also, the code allows a pin by pin analysis of the neutronic scalar flux, for each energy group, showing the local differences between successive approximations that are not fully appreciated from the assembly power distribution.

In future works the implementation of higher order time discretization schemes and the code optimization and parallelization will be addressed.

Acknowledgements

This work was partially supported by the Spanish Agencia Estatal de Investigación under project ENE2017-89029-P-AR, and the Generalitat Valenciana under project PROMETEO/2018/035. The authors express their gratitude to the anonymous reviewers for their suggestions and helpful comments.

References

[1] A.F. Henry, Nuclear-Reactor Analysis, MIT Press, Cambridge, 1975.
[2] R. McClarren, Theoretical aspects of the simplified P_n equations, Transport Theor. Stat. 39 (2011) 73–109.
[3] B. Davison, Neutron Transport Theory, Oxford University Press, London, 1957.
[4] M. Clark Jr., K.F. Hansen, Numerical Methods of Reactor Analysis, New York Academic, New York, 1964.
[5] M. Capilla, C.F. Talavera, D. Ginestar, G. Verdú, A nodal collocation method for the calculation of the lambda modes of the P_L equations, Ann. Nucl. Energy 32 (2005) 1825–1853.
[6] M. Capilla, C.F. Talavera, D. Ginestar, G. Verdú, Application of a nodal collocation approximation for the multidimensional P_L equations to the 3D Takeda benchmark problems, Ann. Nucl. Energy 40 (2012) 1–13.
[7] W.M. Stacey, Nuclear Reactor Physics, WILEY-VCH Verlag GmbH & Co., KGaA, Weinheim, 2007.
[8] S.I. Heizler, Asymptotic Telegrapher's Equation (P_1) Approximation for the Transport Equation, Nucl. Sci. Eng. 166 (2010) 17–35.
[9] E.M. Gelbard, Applications of spherical harmonics method to reactor problems, Technical Report WAPD-BT-20, Bettis Atomic Power Laboratory, 1960.
[10] E.M. Gelbard, Simplified spherical harmonics equations and their use in shielding problems, Technical Report WAPD-T-1182, Bettis Atomic Power Laboratory, 1961.
[11] E.W. Larsen, J.E. Morel, J.M. McGhee, Asymptotic derivation of the multigroup P_1 and simplified P_N equations with anisotropic scattering, Nucl. Sci. Eng. 123 (3) (1996) 328–342.
[12] M. Frank, A. Klar, E.W. Larsen, S. Yasuda, Time-dependent simplified P_N approximation to the equations of radiative transfer, J. Comput. Phys. 226 (2) (2007) 2289–2305.
[13] E. Olbrant, E.W. Larsen, M. Frank, B. Seibold, Asymptotic derivation and numerical investigation of time-dependent simplified P_N equations, J. Comput. Phys. 238 (2013) 315–336.
[14] B.G. Carlson, G.I. Bell, Solution of the Transport Equation by the S_N Method, Proc. U.N. Intl. Conf. Peaceful Uses of Atomic Energy, 2nd Geneva P/2386, 1958.
[15] E.E. Lewis, W.F. Miller, Computational Methods of Neutron Transport, John Wiley and Sons, New York, 1984.
[16] R.E. Alcouffe, R.S. Baker, F.W. Brinkley, D.R. Marr, R.D. O'Dell, W.F. Walters, DANTSYS: A diffusion accelerated neutral particle transport code system, LA-12969-M, Los Alamos National Laboratory, 1995.
[17] R.E. Alcouffe, R.S. Baker, J.A. Dahl, et al., PARTISN: a time-dependent, parallel neutral particle transport code system, Tech. Rep. LA-UR-05-3925, 2005.
[18] J.R. Askew, A characteristics formulation of the neutron transport equation in complicated geometries, AAEW-M 1108, United Kingdom Atomic Energy Authority, 1972.
[19] M.J. Halsall, CACTUS, a characteristic solution to the neutron transport equations in complicated geometries, AEEW-R–1291, United Kingdom Atomic Energy Authority, 1980.
[20] B. Kochunas, M. Hursin, T. Downar, DeCART-v2.05 Theory Manual, University of Michigan, 2009.
[21] A. Talamo, Numerical solution of the time dependent neutron transport equation by the method of the characteristics, J. Comput. Phys. 240 (2013) 248–267.
[22] B.L. Sjenitzer, J.E. Hoogenboom, Dynamic Monte Carlo method for nuclear reactor kinetics calculations, Nucl. Sci. Eng. 175 (2013) 94–07.
[23] B.L. Sjenitzer, J.E. Hoogenboom, J.J. Escalante, V.S. Espinoza, Coupling of dynamic Monte Carlo with thermal-hydraulic feedback, Ann. Nucl. Energy 76 (2015) 27–39.
[24] Y.G. Jo, B. Cho, N.Z. Cho, Nuclear reactor transient analysis by continuous-energy Monte Carlo calculation based on predictor-corrector quasi-static method, Nucl. Sci. Eng. 183 (2016) 229–246.
[25] N. Shaukat, M. Ryu, H.J. Shim, Dynamic Monte Carlo transient analysis for the Organization for Economic Cooperation and Development Nuclear Energy Agency (OECD/NEA) C5G7-TD benchmark, Nucl. Eng. Technol. 49 (5) (2017) 920–927.
[26] A.J. Hoffman, J.C. Lee, A time-dependent neutron transport method of characteristics formulation with time derivative propagation, J. Comput. Phys. 307 (2016) 696–714.
[27] D. Ginestar, G. Verdú, V. Vidal, R. Bru, J. Marín, J.L. Muñoz-Cobo, High order backward discretization of the neutron diffusion equation, Ann. Nucl. Energy 25(1-3) (1998) 47–64.
[28] S. Goluoglu, H.L. Dodds, A Time-Dependent, Three-Dimensional Neutron Transport Methodology,. Nuclear Science and Engineering, 139(3) (2001) 248–261
[29] S. Dulla, E.H. Mund, P. Ravetto, The quasi-static method revisited, Prog. Nucl. Energ. 50 (8) (2008) 908–920.
[30] R. Miró, D. Ginestar, G. Verdú, D. Hennig, A nodal modal method for the neutron diffusion equation. Application to BWR instabilities analysis, Ann. Nucl. Energy 29 (10) (2002) 1171–1194.
[31] A. Carreño, A. Vidal-Ferràndiz, D. Ginestar, G. Verdú, Modal methods for the neutron diffusion equation using different spatial modes, Prog. Nucl. Energ. 115 (2019) 181–193.
[32] A. Hébert, Development of the nodal collocation method for solving the neutron diffusion equation, Ann. Nucl. Energy 14 (10) (1987) 527–541.

[33] T. Downar, Y. Xu, V. Seker, PARCSv3.0 Theory Manual, UM-NERS-09-001, October,2009.
[34] R. Courant, D. Hilbert, Methods of Mathematical Physics, Vol. I, Wiley-Interscience, 1962.
[35] Wm. H. Reed, Spherical harmonic solution of the neutron transport equation from discrete ordinate codes, Nucl. Sci. Eng. 49 (1972) 10–19.
[36] M. Capilla, C.F. Talavera, D. Ginestar, G. Verdú, A nodal collocation approximation for the multidimensional P_L equations - 2D applications, Ann. Nucl. Energy 35 (2008) 1820–1830.
[37] M.T. Capilla, C.F. Talavera, D. Ginestar, G. Verdú, Nodal collocation method for the multidimensional P_L equations applied to neutron transport source problems, Ann. Nucl. Energy 87 (2016) 89–100.
[38] J.E. Morel, B.T. Adams, T. Noh, J.M. McGhee, T.M. Evans, T.J. Urbatsch, Spatial discretizations for self-adjoint forms of the radiative transfer equations, J. Comput. Phys. 214 (2006) 12–40.
[39] M.M.R. Williams, J. Welch, M.D. Eaton, Relationship of the SPN_A_N method to the even-parity transport equation, Ann. Nucl. Energy 81 (2015) 342–353.
[40] H. Greenspan, C.N. Kelber, D. Okrent, Computing Methods in Reactor Physics, Gordon & Breach Science Publishers, New York, 1968.
[41] A. Pautz, A. Birkhofer, DORT-TD: A Transient Neutron Transport Code with Fully Implicit Time Integration, Nucl. Sci. Eng. 145 (2003) 299–319.
[42] G. Verdú, D. Ginestar, V. Vidal, J.L. Muñoz-Cobo, 3D λ modes of the neutron diffusion equation, Ann. Nucl. Energy 21 (7) (1994) 405–421.
[43] E.R. Shemon, M.A. Smith, C. Lee, PROTEUS-SN Methodology Manual, Nuclear Engineering Division, Argonne National Laboratory, ANL/NE-14/5, https://publications.anl.gov/anlpubs/2014/08/79163.pdf, 2014.
[44] X.S. Li, J.W. Demmel, J.R. Gilbert, iL. Grigori, M. Shao, I. Yamazaki, SuperLU Users' Guide. Lawrence Berkeley National Laboratory, LBNL-44289, http://crd.lbl.gov/xiaoye/SuperLU/, 1999.
[45] Y. Saad, SPARSKIT: a basic tool kit for sparse matrix computations-Version 2, http://www-users.cs.umn.edu/ saad/software/SPARSKIT, 1994.
[46] K.R. Olson, D.L. Henderson, Numerical benchmark solutions for time-dependent neutral particle transport in one-dimensional homogeneous media using integral transport, Ann. Nucl. Energy 31 (2004) 1495–1537.
[47] Argonne Code Center: Benchmark Problem Book, ANL-7416, Supplement 1. Identification 6: Infinite Slab Reactor Model, 1969.
[48] L.A. Hageman, J.B. Yasinsky, Comparison of alternating direction time-differencing methods and other implicit methods for the solution of the neutron group diffusion equations, Nucl. Sci. Eng. 38 (1969) 8–32.
[49] J. Kotchoubey, POLCA-T Neutron Kinetics Model Benchmarking, MA thesis, AlbaNova University Center, KTH Royal Institute of Technology, Division of Nuclear Reactor Technology, 106 91 Stockholm, Sweden, 2015.
[50] A.E. Aboanber, Y.M. Hamada, Computation accuracy and efficiency of a power series analytic method for two- and three- space-dependent transient problems, Prog. Nucl. Energ. 51 (2009) 451–464.
[51] K.S. Smith, An Analytic Nodal Method for Solving the Two-Group, Multidimensional, Static and Transient Neutron Diffusion Equations. Master's Thesis, Massachusetts Institute of Technology, 1979.
[52] S. Zhang, B. Zhang, P. Zhang, H. Yu, Y. Chen, 2018. A nuclear reactor transient methodology based on discrete ordinates method. Sci. Technol. Nucl. Ins. vol. 2014. Article ID 491048, 9 pages. https://doi.org/10.1155/2014/491048.
[53] M. Capilla, D. Ginestar, G. Verdú, Applications of the multidimensional P_L equations to complex fuel assembly problems, Ann. Nucl. Energy 36 (2009) 1624–1634.
[54] C. Cavarec, J.F. Perron, D. Verwaerde, J.P. West, Benchmark calculations of power distributions within assemblies, Nuclear Energy Agency Commitee on Reactor Physics, HT-12/94006 A, NEA/NSC/DOC (94), 28, 1994.
[55] V.F. Boyarinov, P.A. Fomichenco, J. Hou, K. Ivanov, A. Aures, W. Zwermann, K. Velkov, Deterministic Time-Dependent Neutron Transport Benchmark without Spatial Homogenization (C5G7-TD), Version 1.6, NEA/NSC/DOC(2016), OECD Nuclear Energy Agency, 2016.
[56] K.S. Smith, Assembly homogenization techniques for light water reactor analysis, Prog. Nucl. Energ. 17 (1986) 303–335.
[57] M.T. Capilla, C.F. Talavera, D. Ginestar, G. Verdú, Numerical analysis of the 2D C5G7 MOX benchmark using P_L equations and a nodal collocation method, Ann. Nucl. Energy 114 (2018) 32–41.